Doctoral thesis

Multi-electron processes in atoms and molecules

Experimental investigations by coincidence spectroscopy

Author:

Jonas Andersson

UNIVERSITY OF
GOTHENBURG

Department of Physics
Faculty of Science
University of Gothenburg
Gothenburg, Sweden 2019

Doctoral Dissertation in Physics

Department of Physics
University of Gothenburg
412 96 Gothenburg, Sweden

Main supervisor:
Prof. Raimund Feifel, Department of Physics, University of Gothenburg
Examiner:
Prof. Ann-Marie Pendrill, Department of Physics, University of Gothenburg
Opponent:
Prof. Reinhard Dörner, Institut für Kernphysik, Goethe Universität

ISBN: 978-91-7833-484-1 (printed)
ISBN: 978-91-7833-485-8 (pdf)
URL: http://hdl.handle.net/2077/59899

Cover: Electron wavefunctions of hydrogenic orbitals.

Printed by BrandFactory, Kållered, 2019
Typeset in LaTeX

Abstract

This thesis presents studies on multi-electron processes in atoms and molecules initiated by single-photon absorption. The experimental techniques used for these studies rely on synchrotron radiation offered at large scale user facilities, and a magnetic bottle spectrometer. The magnetic bottle spectrometer is a versatile time-of-flight instrument that collects charged particles emitted from an ionization event using a characteristic magnetic field. The experiments were carried out in a coincidence detection mode, which allows selective analysis of correlated ionization processes.

The work in this thesis includes detailed analyses of Auger decay processes leading to triply ionized final states in atomic Cd and Hg. The experimental data were compared with numerical calculations to identify the triply ionized final states and the Auger cascades leading to these states. The Auger cascade analyses identified important intermediate inner-states involved in the formation of triply ionized final states, and demonstrated the strong influence of Coster-Kronig transitions when energetically allowed. The studies on Cd also demonstrated the involvement of shake-up transitions in reaching the triply ionized ground state from photoionization using 200 eV photons.

A new instrument for multi-electron and multi-ion coincidence studies was developed and used in experimental studies on Auger cascades in atomic Xe and on Coulomb explosion of molecular ICN. We studied the final charge state distributions from photoionization of different subshells in Xe, by measuring the ion mass spectra recorded in coincidence with specific photoelectrons. These results were compared with experimental results on Coulomb explosion of ICN from photoionization of similar subshells in I. The results suggest that the overall degree of ionization in Coulomb explosion of ICN is similar to the charge state distributions from photoionization of the related subshells in Xe.

Furthermore, experimental results on energy sharing distributions of the two emitted electrons from single-photon direct double photoionization of He are presented. Energy sharing distributions were measured by recording the kinetic energies of both electrons in coincidence for excess energies ranging from 11-221 eV. An empirical model was introduced to parametrize the shapes of the distributions and to form benchmarks for future studies on other direct double ionization processes. The experimental distributions were used to extract indirect information on the knock-out mechanism, thought to be partly responsible for the direct double photoionization process. Theoretical shake-off distributions and the experimentally estimated knock-out distributions were parametrized using the same empirical model, and the results are found to be in agreement with numerical simulations.

Svensk populärvetenskaplig sammanfattning

Idag vet vi att den materia vi stöter på i vår vardag består av atomer. En atom är ett system av negativt laddade elektroner som är bundna till en positivt laddad kärna av protoner och neutroner. Elektroner och protoner växelverkar med varandra genom den elektromagnetiska kraften, vilket kan leda till att elektroner formerar sig kring en atomkärna. Fysiker insåg vid början av 1900-talet att partiklar beter sig underligt på den mikroskopiska skala som karakteriserar en atom. Klassiska förklaringsmodeller kunde inte beskriva atomens fysik, vilket ledde till uppkomsten av den idag väl erkända kvantfysiken. I den kvantmekaniska världen beskrivs partiklar bäst av matematiska vågfunktioner. Att modellera partiklar med vågfunktioner utgör ett starkt fundament för att beskriva de fascinerande fenomen som särskiljer kvantfysik från klassisk fysik.

En konsekvens av atomära elektroners vågbeteende är att de fördelar sig i olika formationer kring kärnan där de olika formationerna motsvarar olika diskreta energitillstånd. En molekyl bildas i sin tur som följd av de atomära elektronernas struktur och hur deras vågfunktioner samverkar när olika atomära system möts. Molekylära bindningar skapas när vågfunktionerna formerat sig så att attraktionskraften mellan elektronerna och atomkärnorna blir lika stark som den repulsiva kraft som uppstår mellan atomkärnorna. Detta jämviktsläge binder atomära system nära varandra och stabila molekylära system skapas. Molekylära system av elektroner karakteriseras likt atomära system av diskreta energitillstånd som beror på elektronfördelningen. Atomer och molekyler strävar efter att minimera systemets totala energi och den elektronfördelning som motsvarar det lägsta möjliga energitillstånd kallas för systemets grundtillstånd.

Både atomära och molekylära system kan gå från sitt grundtillstånd till ett högre energitillstånd genom att absorbera energi från dess omgivning. Detta kan ske då en atom utsätts för elektromagnetisk strålning. Fotoner representerar en fundamental kvantiserad enhet av det elektromagnetiska fältet och bär med sig en viss diskret energi. När en atom absorberar en foton av tillräckligt hög energi kan det leda till att fotonenergin övergår till kinetisk energi, så att en elektron kan frigöras från kärnans bindande kraft. Denna process fick sin teoretiska förklaring av Albert Einstein år 1905. Upptäckten fick stort genomslag och resulterade i att han tilldelades Nobelpriset i fysik.

Processen kallas för fotojonisation och har studierats flitigt under 1900-talet. Studier på fotojonisation har visat att elektroner binds olika hårt beroende på hur de formerar sig i en atom eller molekyl. Det behövs en högre fotonenergi för att jonisera elektroner från formationer nära kärnan och mindre från formationer långt ifrån. En

elektron som fotojoniserats från en formation nära kärnan lämnar ett tomrum efter sig, vilket gör det kvarvarande systemet av elektroner instabilt. System är lämnat med ett överskott av energi och den totala elektronfördelningen motsvarar inte längre ett grundtillstånd. Elektronerna i systemet påbörjar därför en omfördelningsprocess för att frigöra överskottsenergin. Denna omfördelningprocess kan ske i olika steg, där varje steg kan leda till att fler elektroner frigörs från systemet. Ett sådant steg kallas för ett Augersönderfall och om den totala överskottsenergin är tillräckligt hög kan en kaskad av Augersönderfall uppstå. Augersönderfall går väldigt fort och en kaskadprocess kan transformera ett atomärt system till ett högt positivt laddat system inom loppet av ett par femtosekunder.

Fotojonisation och Augersönderfall kan rubba kraftjämvikten som stabiliserar en molekyl och leda till dramatiska konsekvenser för molekylstrukturen. När mängder av elektroner lämnar ett molekylärt system blir repulsionskraften mellan atomkärnorna plötsligt mycket starkare än attraktionskraften. Denna plötsliga förändring kan leda till att atomkärnorna snabbt accelereras bort ifrån varandra i en explosionliknande process. Processen kallas passande för en Coulomb-explosion och kan leda till att en molekyl plötsligt bryts upp i sina beståndsdelar. En Coulomb-explosion lämnar kvar en mängd separerade positiva och negativa laddningar med hög kinetisk energi, vilket kan leda till strålskador på biologiska material och påverka kemiska balanser högt uppe i vår atmosfär och ute i rymden.

I denna avhandling studeras de kvantmekaniska mekanismer som ligger bakom dessa processer. Vi har undersökt olika jonisationprocesser och experimentellt studerat hur atomer och molekyler påverkas av att absorbera en högenergetisk foton. Våra experiment har utförts vid synkrotronljusanläggningen BESSY II i Berlin, Tyskland, för att få tillgång till högintensiv Röntgenstrålning. En synkrotron är en partikelaccelerator som accelererar elektroner till hastigheter endast en bråkdel ifrån ljusets hastighet. Genom att använda starka magneter kan elektronernas relativistiska rörelse utnyttjas för att generera intensiv Röntgenstrålning av reglerbar fotonenergi. Strålningen fokuseras med speciell Röntgenoptik för att kunna fotojonisera atomer och molekyler och studera de Augersönderfall som följer från elektronernas omfördelningprocess.

De elektroner som frigörs i under denna process mäts genom att använda ett särskilt instrument som fångar upp frigjorda elektroner med hjälp av ett magnetfält. Instrumentet kallas för en magnetisk flaskspektrometer. Namnet härstammar från magnetfältets karakteristiska geometri som påminner om formen av en flaska. Elektronerna fångas upp i öppningen av flaskhalsen, där magnetfältet är som starkast, och rör sig sedan i en spiral bana genom flaskans kropp tills de når botten där en detektor registrerar dem. Flygtiden genom spektrometern ger oss viktig information om elektronernas kinetiska energi, som i sin tur avslöjar hur elektroner stegvis omfördelats i en atom eller molekyl under processen att nå ett nytt grundtillstånd.

Med denna teknik har vi studerat Augersönderfall i atomärt kadmium och kvicksilver. Från dessa studier har vi kunnat identifiera vilka elektronfördelningar som är aktiva vid olika steg av en Augerkaskad och hur sannolikt de övergår till andra tillstånd. Studierna har också påvisat att kaskader av Augersönderfall ofta leder till olika sluttillstånd och att stegprocessen dit varierar. Från studier på xenon och ICN-molekyler har vi också kunnat visa hur dessa processer leder till olika grad av jonisation och att graden av jonisation i en atom sannolikt predikterar vissa aspekter av Coulomb-explosioner i molekyler som innehåller liknande atomer. I studien på atomärt kadmium identifierade vi även intressanta signaler från Augersönderfall som avviker från den stegvisa modellen.

För att bättre förstå processer som avviker från stegmodellen studerade vi även en särskild processs i helium, där båda elektronerna fotojoniseras av en enda foton. Processen är ett grundläggande exempel på hur kvantmekaniska korrelationer påverkar atomära elektroner. Vi studerade processen genom att mäta hur elektronerna delar överskottsenergi från fotonen mellan sig. Mätningarna påvisade hur elektronerna delar energin i ett särskilt systematiskt mönster som beror på fotonens energi. Från vår mätdata kunde vi utveckla en matematisk model som beskriver detta mönster och som kan användas som ett riktmärke för att jämföra liknande processer i andra atomära och molekylära system.

Genom att kombinera vår modell med ett tidigare utvecklat teoretiska ramverket lyckades vi ifrån vår mätdata estimera effekten av de två kvantmekaniska mekanismer som tros ligga bakom processen. Denna estimering gav liknande resultat från det som tidigare predikterats från teoretiska simuleringar, vilket stärker hypotesen och motiverar liknande studier på besläktade processer i andra atomära system. Fortsatt forskning kan förhoppningsvis ge svar på om samma kvantmekaniska mekanismer ligger bakom andra liknande processes som också avviker från den stegvisa modellen.

List of papers

List of papers and manuscripts that this thesis is based on:

I. Triple ionization of atomic Cd involving $4p^{-1}$ and $4s^{-1}$ inner-shell holes
J. Andersson, R. Beerwerth, P. Linusson, J.H.D. Eland, V. Zhaunerchyk, S. Fritzsche and R. Feifel
Physical Review A **92**, 023414 (2015)
My contributions: Project planning, data analysis and writing the manuscript.

II. Auger decay of 4d inner-shell holes in atomic Hg leading to triple ionization
J. Andersson, R. Beerwerth, A. Hult Roos, R.J. Squibb, R. Singh, S. Zagorodskikh, O. Talaee, D. Koulentianos, J.H.D. Eland, S. Fritzsche and R. Feifel
Physical Review A **96**, 012505 (2017)
My contributions: Project planning, conduction of experiments, data analysis and writing the manuscript.

III. Ion charge-resolved branching in decay of inner shell holes in Xe up to 1200 eV
J.H.D. Eland, C. Slater, S. Zagorodskikh, R. Singh, J. Andersson, A. Hult-Roos, A. Lauer, R.J. Squibb and R. Feifel
Journal of Physics B: Atomic, Molecular and Optical Physics **48**, 205001 (2015)
My contributions: Instrument development, conduction of experiments and contributed to the manuscript.

IV. Dissociation of multiply charged ICN by Coulomb explosion
J.H.D Eland, R. Singh, J.D. Pickering, C.S. Slater, A. Hult Roos, J. Andersson, S. Zagorodskikh, R. Squibb, M. Brouard and R. Feifel
The Journal of Chemical Physics **145**, 074303 (2016)
My contributions: Instrument development, conduction of experiments and contributed to the manuscript.

V. Energy sharing distributions in direct double photoionization of He
J. Andersson, S. Zagorodskikh, A. Hult Roos, O. Talaee, R.J. Squibb, D. Koulentianos, M. Wallner, V. Zhaunerchyk, R. Singh, J.H.D. Eland, J.M. Rost and R. Feifel
Submitted to Scientific Reports
My contributions: Project planning, conduction of experiments, data analysis, model development and writing the manuscript.

List of papers and manuscripts that I have contributed to, which are not included in the thesis:

- **Relative extent of double and single Auger decay in molecules containing C, N and O atoms**
  A. Hult Roos, J.H.D. Eland, J. Andersson, S. Zagorodskikh, R. Singh, R.J. Squibb and R. Feifel
  Physical Review A **18**, 25705 (2016)

- **Abundance of molecular triple ionization by double Auger decay**
  A. Hult Roos, J.H.D. Eland, J. Andersson, R.J. Squibb, D. Koulentianos, O. Talaee and R. Feifel
  Scientific Reports **8**, 16405 (2018)

- **Dissociations of water ions after valence and inner-valence ionization**
  A. Hult Roos, J.H.D. Eland, J. Andersson, R.J. Squibb, and R. Feifel
  The Journal of Chemical Physics **149**, 204307 (2018)

- **Relative extent of triple Auger decay in CO and CO_2**
  A. Hult Roos, J. H. D. Eland, J. Andersson, M. Wallner, R. J. Squibb, and R. Feifel
  Physical Chemistry Chemical Physics, accepted April 16 (2019)

- **Experimental transition probabilities for 4p–4d spectral lines in V II**
  H. Nilsson, J. Andersson, L. Engström, H. Lundberg and H. Hartman
  Astronomy and Astrophysics **622**, A154 (2019)

- **Coulomb explosion of CD_3I induced by single photon deep inner-shell ionisation**
  M. Wallner, J.H.D. Eland, R.J. Squibb, J. Andersson, A. Hult Roos, R. Singh, O. Talaee, D. Koulentianos, M.N. Piancastelli, M. Simon, and R. Feifel
  In manuscript

- **Double ionization of atomic Zn**
  J. Andersson, A. Hult Roos, O. Talaee, R.J. Squibb, M. Wallner, R. Singh, J.H.D. Eland, and R. Feifel
  In manuscript

- **Formation and relaxation of K^{-2} and $K^{-2}V$ double-core-hole states in C_4H_{10}**
  D. Koulentianos, R. Couto, J. Andersson, A. Hult Roos, R.J. Squibb, M. Wallner, J.H.D. Eland, M.N. Piancastelli, M. Simon, H. Ågren, and R. Feifel
  In manuscript

Contents

List of Figures

Chapter 1

Introduction

An atom or a molecule in its ground state is a stable system with an internal energy that does not change unless external forces act on it. If a neutral or ionic system is energetically excited to a higher energy state, it will no longer be stable and will energetically relax with time. There are multiple processes that may excite an atomic or molecular system, and there are many ways in which such systems may be excited. Similarly, there are often many ways by which excited states may energetically relax, some rather simple but many very complex. These relaxation processes often involve electronic rearrangement which transforms the system as it goes from one state to another.

An atom or a molecule can become highly excited by absorbing radiation of high energy. Electronic rearrangement of such an excited state, can lead to a sudden release of electrons from the system. In a molecule, this may lead to a fast build-up of unscreened positive charges, which can have dramatic consequences for the molecular structure. Strong repulsive forces between the atomic nuclei can cause the molecule to break up into its constituents, and the process can result in a sudden release of free charges. These processes can have a large impact on the local molecular environment, and initiate secondary chemical reactions that cause significant radiation damage in solids and biological systems.

In order to understand the characteristics of these atomic and molecular processes, we need to rely on accurate experimental measurements to develop our quantum mechanical models. In this thesis, we will study multi-electron processes that follow when an atom or a molecule absorbs a high energy photon. We will present results from our experimental investigations of these processes, and compare the findings with our current models. In this way, we hope that our results lead to a deeper understanding of electronic processes in photoionized systems. The results of these studies are presented in full length in papers I-V, and summarized in a later chapter of this thesis. However, in this chapter, we will first lay a foundation for the subsequent chapters by discussing the most important aspects of the field. We will start by giving a brief overview of important concepts from atomic physics.

1.1 Electronic structure of atoms

Modern understanding of the structure of atoms and molecules relies on a quantum mechanical framework. Finding a wave function, $\Psi(\vec{r}, t)$, that solves the Schrödinger equation

$$i\hbar\frac{\partial\Psi(\vec{r}, t)}{\partial t} = \hat{H}\Psi(\vec{r}, t) \ , \tag{1.1}$$

is generally a key procedure in understanding atomic and molecular systems. The equation describes a given quantum mechanical system in terms of the Hamiltonian operator, $\hat{H}$. The operator describes the total energy and includes both the potential and kinetic energy of the system. The simplest atomic system we can consider is that of hydrogen, where a single electron is bound by proton. Solving the equation for atomic hydrogen, with a Coulomb potential that does not vary in time, provides a complete set of stationary states that describe the system. The spatial part of the solution solves the time-independent Schrödinger equation

$$\left[-\frac{\hbar^2}{2m}\nabla^2 + V(\vec{r})\right]\psi_n(\vec{r}) = E_n\psi_n(\vec{r}) \ , \tag{1.2}$$

where V is the potential energy. The solution gives rise to a an infinite number of eigenstates, ψ_n, with corresponding energy eigenvalues E_n. The solutions that correspond to negative energies are called bound states, as they represent states where the electron is bound to the nucleus. These states give rise to a spectrum of energies, which is often represented in an energy level diagram, as shown in Fig. 1.1. The solutions with positive energies represent scattering states where the electron is 'free' but feels the presence of a positively charged nucleus. These solutions give rise to a continuum of energies, in contrast to the discrete spectrum of bound states. It is therefore common to categorize the states of an atomic system into two groups, the discrete (bound) states and the continuum (free) states.

An atomic system that consists of more than one electron is complicated and the complexity grows rapidly with the number of electrons. The complexity relates to the number of terms in the Hamiltonian that take the Coulomb interaction between the individual electrons into account. A common strategy when dealing with complicated quantum mechanical systems is to describe it in terms of a simpler system with a known solution, that resembles the complicated one. If a proper simplified system, with only a small difference in energy can be found, one may treat the complicated problem approximately in accordance with *perturbation theory*. However, the energy contribution from the electron-electron interactions may not always be small. For instance, the energy contribution from the repulsive force between the two electrons in helium is $\sim 27\%$ of the total energy [1, 2]. The contribution is even more important when considering the full effect of all electron-electron interactions in a heavy atom. We therefore need to

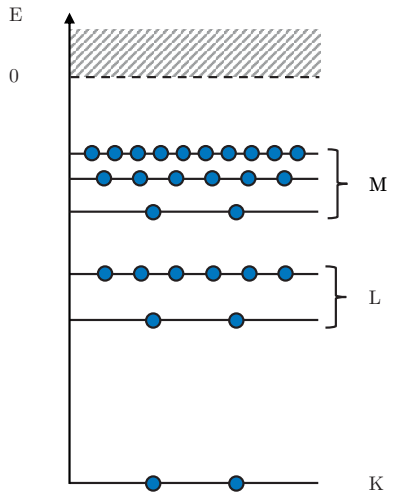

Figure 1.1: Energy level diagram describing eigenvalues of the energy for solutions to a central field approximated Schrödinger equation.

rely on other approximation methods as well. A common approach is to observe that the quantity $1/\left|\vec{r}_{\mathrm{a}}-\vec{r}_{\mathrm{b}}\right| = 1/r_{\mathrm{ab}}$, which defines the repulsive potential between two electrons a and b, can be accounted for by splitting the interaction in one radial and one tangential part [3]. In many cases, the radial component becomes the dominant contributor in the electron-electron interaction. By averaging this radial contribution, one may approximate it as an additional radially symmetric field that effectively screens the central field from the nucleus. This method is called the *central field approximation* and solving the Schrödinger equation under this approximation results in wave functions and energies that depend on the quantum numbers n and l. This approximation serves as a foundation for many computational techniques [4] and the quantum numbers n and l define important terminology and notational conventions used in atomic spectroscopy. A given n-value is usually referred to as an *electron shell*. In chemistry and X-ray spectroscopy, it is common to refer to different shells using the letter notations:

n:	1	2	3	4	6	$\cdots$
	K	L	M	N	O	$\cdots$

A given combination of n and l is generally referred to as an *atomic orbital* and refers to a single-electron wave function. The convention for denoting an atomic orbital is to use the numerical value of n and a spectroscopic notation for the value l. The logic is the following:

l:	0	1	2	3	4	$\cdots$
	s	p	d	f	g	$\cdots$

The *electron configuration* of an atom describes the electron distribution and which orbitals are occupied. The ground state configuration of carbon is for instance $(1s)^2(2s)^2(2p)^2$. The superscript number refers to the number of electrons that occupy a specific orbital. Each atomic orbital may in turn be grouped into states that depend on the magnetic quantum number of m_l, which can take $2l + 1$ values for each orbital. Each combination of n, l and m_l can fit two electrons with opposite spin. For instance, two electrons may occupy an ns orbital, six electrons may occupy an np orbital and ten electrons may occupy an nd orbital.

The notations mentioned above are useful but they do not tell the whole story about the electronic structure of multi-electron atoms. Referencing single-electron wave functions when describing multi-electron atoms is a convenient but sometimes rather rough approximation. There are several other effects to consider, such as more complex electron-electron interactions and effects related to spin-orbit interactions. Even relativistic effects become important to consider in some cases. Important to this thesis is the combined effect of many electrons and how they couple and *correlate* before and during electronic processes in the atomic system. Multi-electron relaxation processes typically relate to the Coulomb interaction between the electrons and can lead to many different phenomena. However, for an atom or a molecule to give rise to any relaxation phenomena, some perturbation must first excite the system into an unstable state.

1.2 Interactions with electromagnetic radiation

When a photon interacts with an atom or a molecule, there is a probability that the photon may be absorbed by the system. The energy that is added to an atom or a molecule by an absorbed photon can lead to electronic rearrangements in the system. The type of rearrangements that can occur when a photon is absorbed vary and the set of possible final states given by a photon absorption can be very large. The most accurate way to calculate the transition probabilities would be to calculate the time-dependent dynamics of the entire system. However, this is often not feasible and approximated treatments are required. It turns out that the electronic rearrangement can, in many cases, be treated in a step-wise manner, where the first step is a single electron transition induced by the photon. Which electrons are most likely to interact with the incoming photon is set by how well they resonate with the photon frequency. A resonance occurs when the energy of the photon matches the difference between two energy eigenvalues of the system. An *excitation* occurs when the resonance leads to a transition between two bound states and a *photoionization* occurs when the photon energy is high enough that it brings the system to states in the continuum of positive energy levels. Simple schematic illustrations of the two types of photon-induced transitions are shown in Fig. 1.2.

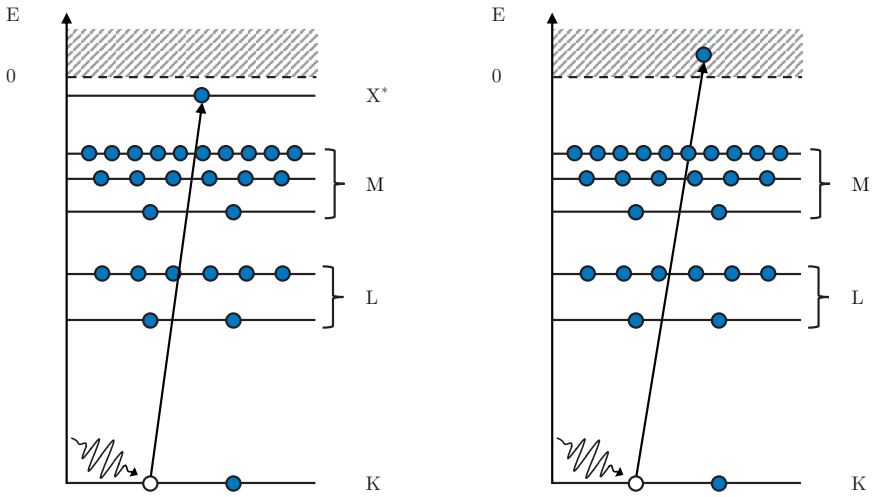

(a) **(b)**

Figure 1.2: An absorbed photon may lead to either a) an inner-shell excitation or b) inner-shell ionization, depending on the energy.

To the extent that the independent particle model is valid, one can describe the intermediate state in terms of a missing electron, often referred to as a *vacancy* or a *hole*, in the state that the interacting electron previously occupied. An inner-shell vacancy, located deep down in the energy level structure of a multi-electron system, indicates that the system has been brought to an unstable and highly excited state. It will hence undergo a relaxation process, which may lead to different final states through a variety of possible *relaxation* processes.

1.3 Electronic relaxation

Once an inner-shell vacancy has been created in the system, it will relax by rearranging its electronic structure and fill the vacancy, thereby minimizing the energy. There are generally two competing mechanisms by which the rearrangement may occur. One is by radiative decay, where the system relaxes energetically by single-electron rearrangement and the emission of a photon. When a hole-state with a vacancy in a core or inner-shell orbital decays radiatively, the photon energy is usually in the X-ray range. The transition is hence often referred to as an X-ray fluorescence decay. The other decay mechanism is a non-radiative decay called Auger decay.

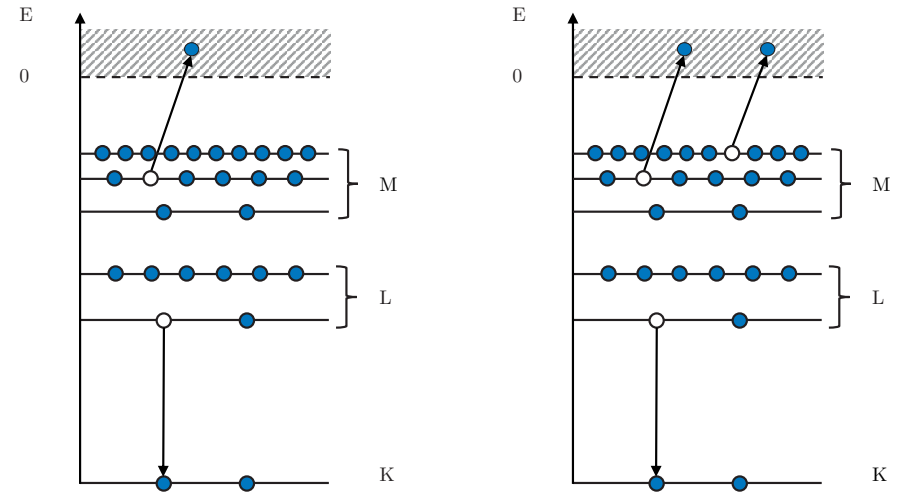

Figure 1.3: a) Example of a single Auger decay and b) example of a direct double Auger decay.

1.3.1 Auger decay

The simplest picture of an Auger decay is similar to an X-ray fluorescence decay in the sense that an electron from a higher orbital fills the vacancy. However, instead of having the excess energy emitted in the form of a photon, the system can release a secondary electron from a higher orbital into the continuum. The kinetic energy of the emitted electron corresponds to the energy difference of the singly charged hole-state and the doubly charged final state. The transition rate, W, of an Auger decay between an initial state, i, and a final state, f, can be estimated using Fermi's Golden Rule [5–7]

$$W_{i\to f} = \frac{2\pi}{\hbar}\left|\left\langle \Psi_f \middle| \frac{1}{r_{\mathrm{ab}}} \middle| \Psi_i \right\rangle\right|^2 \rho(E_f) \ , \tag{1.3}$$

where ρ is the density of final states with an electron in the continuum. The Coulomb interaction makes it more likely that the Auger effect involves two electrons that are spatially close. Hence, in describing the process in an independent particle energy level structure, such as in Fig. 1.3a, it is generally more likely that the hole moves upwards in a small step rather than a long step, as long as the released energy is sufficient to release the secondary electron. In rare cases, more complicated Auger decays involving three active electrons can occur. This resembles a single Auger decay but some of the excess energy is used to bring a third electron to an excited state which, if the energy is sufficiently high, may lie in the continuum. This process was first observed by Carlson et. al. in 1965 [8] and is called *direct double Auger decay*. It leads to the simultaneous

release of two electrons and the process is illustrated schematically in Fig. 1.3b. In contrast to the single Auger decay, the direct double Auger decay is characterized by a fixed kinetic energy sum of the two released electrons. However, the kinetic energy of each of the two electrons can vary and the process gives rise to a continuous kinetic energy distribution of the two Auger electrons.

1.3.2 Decay cascades

A completed Auger decay typically leaves the system with an additional positive charge due to the newly generated orbital vacancy. The vacancy that initiated the Auger decay has moved to a new orbital of lower binding energy, reducing the overall energy of the system. The system has relaxed in energy but may still be in a configuration corresponding to a highly excited state. If the system is far from having reached a new stable state, the relaxation process may continue with a new relaxation step being either a new Auger decay or a fluorescence decay. A single vacancy deep down in the level structure of a heavy atom can therefore decay through a complicated network of possible decay channels. A five-step decay example is shown in Fig. 1.4. At each node in the network, there is a trade-off probability for whether the next decay will be a fluorescence decay or an Auger decay. The nodes at the bottom of the diagram describe how many electrons that have left the system during the decay process, i.e. which ionic charge state that was produced. Given a certain number of decay steps, most charge states can typically be reached via different routes or combinations of radiative and non-radiative steps, which leads to a statistical weight for each charge state. The trade-off probability for each step depends on the atomic number, Z, and varies for each node, i.e. electronic state, in the network [9–11].

For most intermediate shells, Auger decay becomes the dominant process and the relative probability of fluorescence decay negligible. However, some intermediate states can, due to energy conservation rules, be forbidden to relax by Auger decay. This is illustrated schematically in Fig. 1.5a, which describes how a network of Auger cascades passes through different charge states. The black arrows at each step in the network denote Auger decays leading to states that are allowed to relax further by Auger decay, whereas the red arrows denote Auger decays to states that are not. The number of black and red arrows varies throughout the network and the relative number at each step defines the output probability for each charge state. A hypothetical example of a charge state distribution output from such network is illustrated in Fig. 1.5b. The charge state distributions depend on combinatorial aspects of how a given number of holes can be distributed in the ionic system of each step in the network, and how many of those combinations are allowed to relax further by Auger decay. More complicated

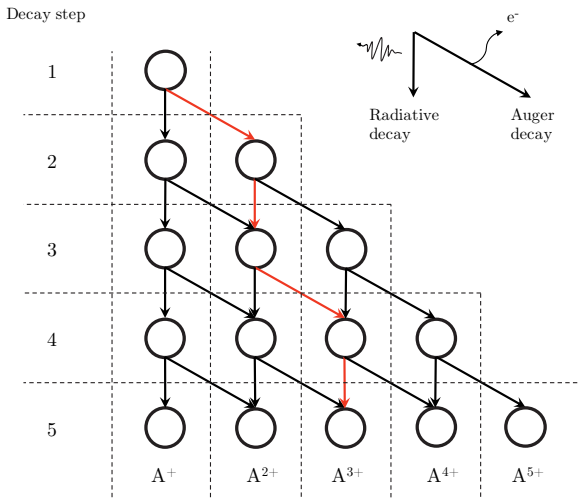

Figure 1.4: Network illustrating the trade-off between radiative decay and Auger decay at each step of a five-step relaxation. The vertical transitions correspond to radiative decays that move vacancies upward in the energy level structure without changing the net charge of the system. The downward tilted arrows correspond to Auger decays that result in an additional positive net charge of the system. The red arrows illustrate one of multiple channels leading to three-fold ionization.

processes, such as direct double Auger decay and shake-off mechanisms, a process we will return to later in section 1.4, can also be important and complicate the relaxation network further.

Modelling all channels in a cascade requires a high level of theoretical and computational accuracy in each step of the process. The relaxation process of a 1s vacancy in a heavy atom, such as Hg with 80 electrons, requires calculating accurate wave functions and energies for an enormous number of quantum states. The wave functions need to be coupled accurately to obtain each part of an immensely complex network of transition amplitudes. Each part of the chain depends on the previous one and errors accumulate throughout the network. As every computational model involves some degree of approximation, either numerical or physical, there will occur difficulties at some point when modelling a complicated Auger cascade. It is for this reason important to form benchmarks from experimental data to obtain valuable insights into which physical aspects that are most relevant for a given relaxation network.

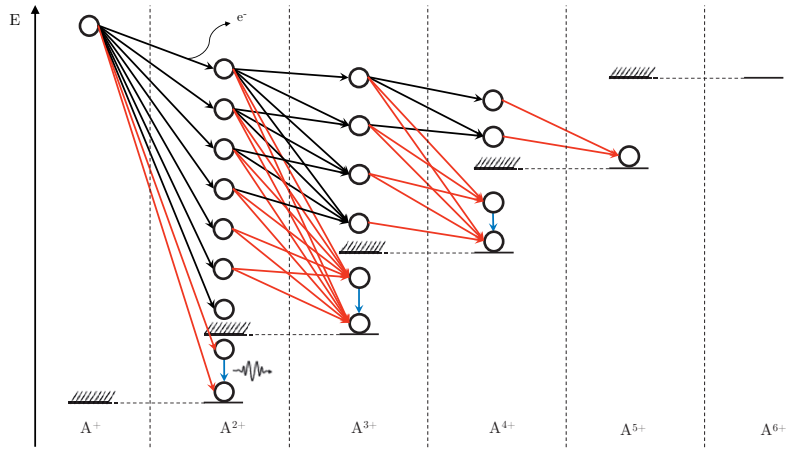

(a)

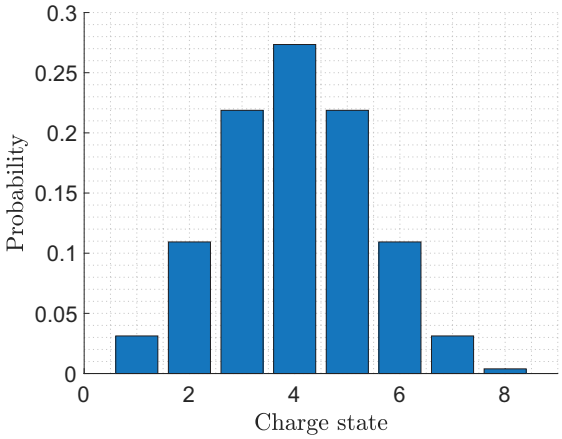

(b)

Figure 1.5: a) Relaxation network of various Auger cascades leading to different charge states. Each node represents a state or groups of states with similar energy. Black arrows denote Auger decays to states that are energetically allowed to relax further by the Auger mechanism, red arrows denote Auger decays to states that are energetically forbidden to decay to higher charge states and blue arrows denote radiative decays. b) Example of a produced charge state distribution based on the relative number of decay channels between each charge state.

1.3.3 Molecular fragmentation

The stability of molecular systems relies on the electronic structure, with some molecular orbitals being more responsible for the inter-atomic bonds than others. These bonding orbitals are often found in the outermost shells. A hole in a core or inner-shell orbital does not directly affect the molecular form much. However, subsequent decay cascades can move holes upward in the energy level structure, which may eventually affect the valence region. As seen above, Auger decays add new vacancies to the system, which may lead to a large number of broken bonds and a quick build-up of un-screened positive charges. This can initiate a so-called *Coulomb explosion*, which is a rather violent breakup of a molecule from strong repulsive forces between the moieties. The strong repulsive force may cause a molecule to fragment into its constituents with a large kinetic energy release.

1.3.4 Breakdown of the step-wise Auger decay

The schematic illustration of an Auger decay, such as in Fig. 1.3a is effective for constructing an intuition of the electronic rearrangement. The decay model with each step being independent of the other works relatively well for most Auger cascades. However, it is important to point out that the correlations that are present before and during the decay cascade might not allow decoupling each step as independent of the other. Generally, the longer the lifetime of a hole-state, the better this approximation holds.

The lifetime relates inversely to the sum of the transition rates to all allowed final states. Some atoms have orbital structures that allow Auger decays where the vacancy is filled by an electron from the same shell. This is a relatively rare decay that is usually not energetically allowed. The decay is called a *Coster-Kronig* decay which, when energetically allowed, can lead to very high transition rates [12]. If also the emitted electron belonged to the same shell, the decay is referred to as a *super* Coster-Kronig decay. The strong transition probabilities of these decays relate to the radial wave functions, which can be very similar within the same shell. Coster-Kronig decays are consequently characterized by short lifetimes, sometimes orders of magnitude shorter than normal Auger decays [13]. Rapid Coster-Kronig decays are characterized by unusually broad features in conventional electron spectra [13, 14], since a short lifetime, τ, corresponds to a large spread in energy, ΔE, according to the uncertainty principle,

$$\tau \Delta E \geq \frac{\hbar}{2} \, . \tag{1.4}$$

The influence of Coster-Kronig decays can in extreme cases lead to processes that appear very similar to direct double electron emissions.

Another process where the step-wise model fails is when an Auger electron interacts with a slow photoelectron. When the kinetic energy of the photoelectron is close to zero, it may be overtaken by the fast Auger electron. As the Auger electron passes the slow photoelectron, the two electrons can interact and share energy. The fast Auger electron is screened from the residual ionic system by the slow photoelectron, whereas the slow electron may feel a retarding pull from the ion, due to the lost electrostatic screening provided by the Auger electron. These phenomena is often referred to as post-collision interactions (PCI) [15–17]. The extra energy can be directly observed as a positive shift in energy of the Auger electrons and an negative shift for the photoelectrons, both with an additional spectral line broadening [18]. The PCI process implies that the independent step-wise treatment is not completely valid as the Auger process is dependent on the photoelectron.

1.4 Single-photon direct double ionization

A single photon of sufficiently high energy, may bring an atom or molecule directly to a doubly ionized state. This is an interesting process called *single-photon direct double ionization*. There are different types of direct double photoionization processes, which are often categorized according to the orbital origin of the two involved electrons. For instance, three categories of direct double ionization are illustrated in Fig. 1.6. The three categories are often referred to as *double-core* ionization, *core-valence* ionization and *double-valence* ionization. The single-photon direct double ionization process is completely dependent on electron correlations. The process is therefore important for testing our understanding of electronic correlations and it has naturally attracted a lot of attention from both theorists and experimenters [19–25].

An elegant theoretical framework for the process was developed by Pattard et. al. [26, 27] and Schneider et. al. [24, 25]. In 2002, Schneider et. al. [24] proposed a new approach in modelling and conceptualizing the process in He. The approach is based on two different mechanisms that both lead to double ionization. The first mechanism is based on a semi-classical idea that the primary electron, the one that interacts with the photon, transfers some of its energy to the secondary electron by a collision-like interaction. The collision leads to double ionization if the excess energy is shared so that both electrons receive a kinetic energy that allows them to escape. This collision-like mechanism is called the knock-out (KO) mechanism.

The second mechanism, called the shake-off (SO) mechanism, is a purely quantum mechanical process. It is most rigorously defined when the excess energy is very high. The primary electron can thus be approximated as having left the system instantly, without interacting with the secondary electron as it leaves. The wave function of the secondary electron corresponds to an eigenstate of the Hamiltonian before the photon

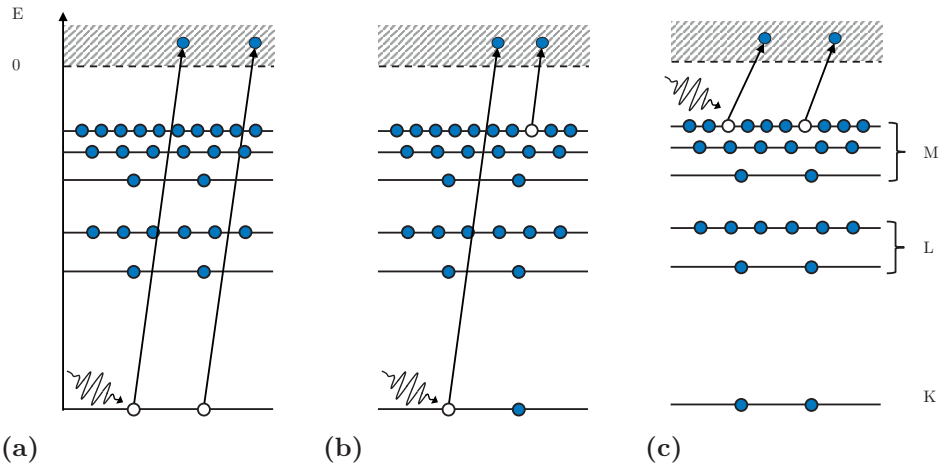

Figure 1.6: Three categories of single-photon direct double ionization. a) Double-core ionization, b) core-valence ionization and c) double-valence ionization.

was absorbed, and will thus not correspond to an eigenstate of the new, instantly changed Hamiltonian. This will cause the wave function of the secondary electron to collapse into one of the energetically accessible eigenstates of the new Hamiltonian. If the photon energy is higher than the double ionization potential, there will be some probability that the secondary electron wave function collapses into a state in the continuum.

Pattard et. al. [26, 27] formulated the total transition amplitude for the direct double photoionization process in terms of two separate transition amplitudes

$$a_{f,i} = a_{f,i}^{\mathrm{KO}} + a_{f,i}^{\mathrm{SO}} \ , \tag{1.5}$$

representing the KO and SO mechanisms, respectively. Taking the modulus squared of Eq. 1.5, one gets

$$|a_{f,i}|^2 = \left|a_{f,i}^{\mathrm{SO}}\right|^2 + \left|a_{f,i}^{\mathrm{KO}}\right|^2 + C_{\mathrm{int}} \ , \tag{1.6}$$

where C_{int} describes the interference between the two mechanisms. The interference term was found to be mostly negligible in the case of He, and the error from neglecting it was estimated to only account for at most a few percent of the total cross section [24].

In the above definition, the KO mechanism takes all *post-absorption interactions* (PAI) into account, while the SO mechanism depends solely on the initial state correlations. Shake-off from an ns state, as the ground state of the typical test case of He, is characterized by the primary electron going out as a p-wave, as it takes the angular momentum of the absorbed photon. The secondary shake-electron does not change its angular momentum and goes consequently out as an s-wave. The KO mechanism has no such restrictions, as angular momentum may be shared arbitrarily between the electrons.

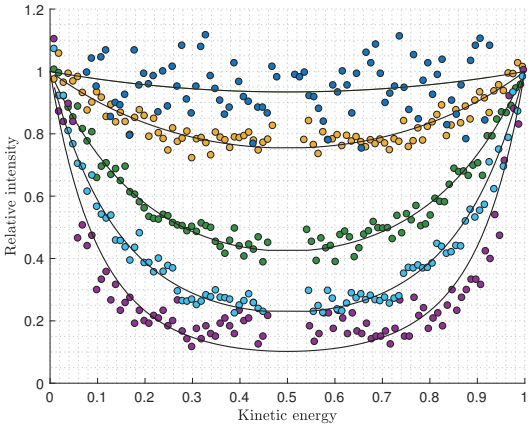

Figure 1.7: Energy sharing distributions measured at five different excess energies. The curves from top to bottom represents distributions obtained at excess energy 11, 51, 101, 161 and 221 eV, respectively.

An interesting question is in which way the two electrons share the available excess energy. The total sharing distribution is made up by two partial distributions (assuming $C_{\text{int}} = 0$), related to the KO and the SO mechanisms. It is known that the energy sharing distribution of He takes on a form that gradually changes from being nearly flat, for low excess energies, to ∪-shaped as the available excess energy increases. This can be seen in Fig. 1.7, which shows a sample of measured distributions for He. The partial KO and SO distributions both turn gradually from flat to ∪-shaped as the excess energy increases, but with different rates. The relative probability of KO and SO changes with excess energy, hence their relative contribution to the total distribution varies. The KO mechanism is dominant for excess energies up to about 300 eV but becomes less probable at higher energies [24, 25].

The wave collapse that leads to the SO mechanism may also lead the system into various states with the primary electron in the continuum but with the secondary electron still bound to the nucleus. The secondary electron may thus either be found in the ground state of the new Hamiltonian (single ionization) or having been 'shaken up' (SU) into an excited state. Similarly, the excited singly charged final states may be reached by dynamical post-absorption interactions where the secondary electron is 'knocked up' (KU) into an excited state by the primary electron [28].

A simple system such as He will thus have a network of possible relaxation paths that it may evolve through given that a photon was absorbed. Figure. 1.8 illustrates an example of a network of possible relaxation amplitudes for a He-like system. The figure shows how the network branches into certain channels and sub-channels. The

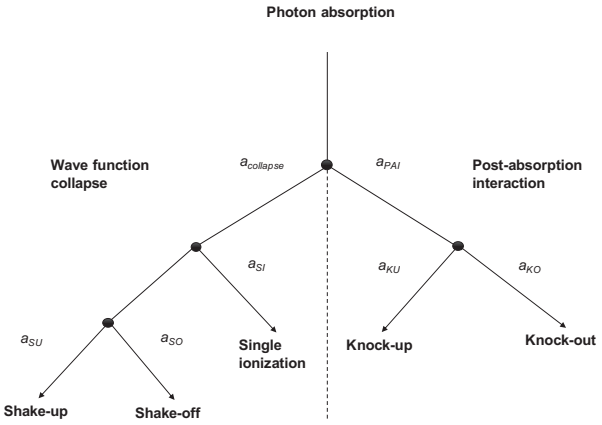

Figure 1.8: Network diagram that exemplifies a logical decision tree of possible relaxation amplitudes, a, after a He atom has absorbed a photon with energy above the double ionization threshold.

initial channel splits into two subsets based on whether or not the primary electron interacted and shared energy with the secondary electron on its way out. The events that involve dynamical PAI are grouped together on the right half of the diagram. The left side of the diagram refers to transition amplitudes that only depend on initial state correlations.

The concepts of KO and SO together constitute an effective framework for understanding direct double photoionisation of He under the dipole approximation. In addition to the SO and KO mechanisms, Amusia et. al. predicted a third *quasifree* mechanism (QFM) [29], which was confirmed experimentally by Schöffler et. al. in 2013 [30]. The QFM mechanism is a small contribution to the non-dipole part of the direct double ionization process, and is characterized by the two electrons being emitted back to back with similar kinetic energies. However, for a photon energy of 800 eV, the non-dipole part amounts to $\sim 1\%$ of the total direct double ionization cross section in He [30], and the contribution from the QFM mechanism is thus very small for lower photon energies.

Other direct processes, such as core-valence photoionization and direct double Auger decays, resemble that of the prototypical example of He. Studying these processes in terms of KO and SO could potentially lead to new insights about direct double ionization processes. Further studies are needed to test how applicable the KO and SO concepts are to systems other than He. We will later in this thesis present an experimental study on direct double photoionization of He, aimed at laying a foundation for extended studies on direct processes. However, in the next chapter, we will first go through the experimental techniques that underlie the studies presented in this thesis.

Chapter 2

Experimental techniques

The velocity of a photoelectron carries information about how tightly it was bound in the atomic system before the photon was absorbed. As the total energy before and after the interaction must be preserved, one can indirectly obtain information about the binding energy of an electron from the photon energy and the kinetic energy of the ejected electron. This was first explained by Albert Einstein with the equation

$$E_{\text{kin}} = E_{\text{photon}} - E_{\text{bind}} \ , \tag{2.1}$$

formalizing his theoretical explanation of the photoelectric effect [31]. When probing multi-ionization processes, it is vital to detect as many of the released particles as possible, since each particle carries some information about the ionization process.

Modern research on electron spectroscopy often targets multi-electron processes that rely on selective orbital ionization. Selective photoionization of inner-shell orbitals requires radiation with high wavelength accuracy and tunable photon energies in the range of UV to hard X-rays. This is often offered at modern synchrotron facilities, and the work that this thesis is based on would not be possible without the use of synchrotron radiation. Synchrotron radiation sources can vary in design since the primary objective for each machine may differ. However, synchrotron facilities generally offer radiation with a high light pulse repetition rate, a high intensity and a high photon energy tunability over a very large range of photon energies.

Since synchrotron radiation facilities have been the primary light source for the present studies, we will in the following section give a brief overview of their most important aspects of operation. The two subsequent sections will discuss the experimental techniques used for detecting particles released from an atomic or molecular system after the absorption of a photon. Finally in this chapter, a few key experimental principles and analysis techniques will be discussed, all important for extracting and distilling as much information as possible from each particle detection.

2.1 Synchrotron radiation facilities

To photoionize electrons bound in the inner-shells of atomic and molecular systems usually requires the use of soft X-ray or hard X-ray photons. In this thesis, we refer to soft X-ray photon energies as ranging from approximately $90 - 1600$ eV, which is

the range of photon energies offered at the two BESSY II beam lines used in this work [32–34]. Photon energies in this range are high enough to ionize 1s electrons in light atoms ($Z \lesssim 10$) as well as electrons in orbitals deep down in the energy level system of heavier systems [35–37]. For instance, a 1 keV photon may ionize an electron as deep down in the system as the 4s orbital in atomic Hg, with the ground state configuration

$$[\mathrm{Ar}]\ 3d^{10}4s^2 4p^6 4d^{10}5s^2 5p^6 4f^{14}5d^{10}6s^2\ .$$

Synchrotron radiation facilities, such as BESSY II in Berlin, offer tunable and high intensity soft X-rays that are well suited for inner-shell ionization. Briefly, the synchrotron accelerates electron bunches to relativistic speeds and stores the relativistic bunches in a storage ring. The storage ring consists of several straight sections forming an approximately circular path for the electron bunches to travel in. Strong bending magnets are used to guide the bunches from one straight section to the next. As the magnetic fields from the bending magnets force the charged bunches to accelerate in new directions, some kinetic energy is converted into electromagnetic radiation. The radiation is comprised of a continuous wavelength spectrum of moderate intensity. The intensity can be substantially enhanced by actively manipulating the electron bunches in a more controlled and variable way. The characteristics of the radiation can in this way be manually set to align with particular experimental aims. Several techniques of manipulating the electron bunches exist, but modern large scale synchrotron facilities generally use so-called *insertion devices* [38].

2.1.1 Insertion devices

The two most common types of insertion devices used at synchrotrons are *wigglers* and *undulators*. The working principles are similar and they both rely on the use of periodic magnet structures that exerts a periodic force on the electron bunch. The magnets are brought close to the path of the electrons with the field lines perpendicular to the bunch velocity. The periodic magnetic field forces the electrons to oscillate tangentially relative to their forward propagation, and the resulting acceleration causes them to radiate. The radiation expands in the forward direction in the shape of a cone due to the relativistic motion of the electrons. The principle is illustrated in Fig. 2.1. The working principles of wigglers and undulators are relatively similar, but since the experimental work in this thesis has only used undulator radiation, we will henceforth limit the discussion to undulators.

Since the electrons travel with approximately the speed of light, a constructive interference pattern occurs between light emitted from different periods in an undulator's magnetic structure. The effect is that the emitted radiation is relatively monochro-

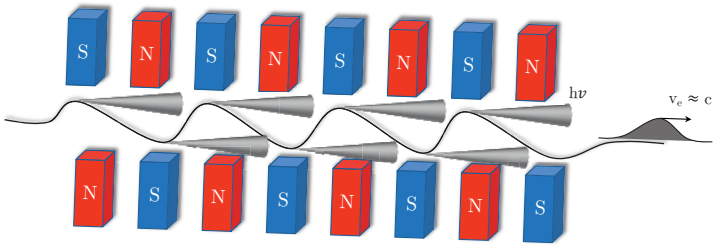

Figure 2.1: Schematic illustration of an undulator.

matic. The emitted wavelength follows approximately [38]

$$\lambda = \frac{\lambda_u}{2\gamma^2}\left(1 + \frac{K^2}{2} + \gamma^2\theta^2\right), \tag{2.2}$$

where λ_u is the period of the magnetic structure, γ the Lorentz factor, θ the angle of observation relative to the direction of propagation and

$$K = \frac{eB_0\lambda_u}{2\pi mc}\ , \tag{2.3}$$

the magnetic deflection parameter. The K parameter is used to differentiate wiggler radiation from undulator radiation. Wiggler radiation is usually defined as when $K \gg 1$ and undulator radiation when $K < 1$ [38].

Undulator radiation is typically linearly polarized as a result of the in-plane oscillation of the electron bunch. It is possible to produce arbitrarily polarized light by using two periodic magnetic structures and phase match the two orthogonally polarized waves. Although undulator radiation is constrained to a much smaller bandwidth than the radiation from the bending magnets, it may still not be small enough for photoionization experiments which target atomic orbitals. Most beamlines are therefore equipped with monochromators, which allow the selection of much more precise wavelengths from the undulator radiation.

2.1.2 Monochromator

Grating based monochromators are typically used for soft X-rays. The wavelengths are dispersed from the grating according to:

$$m\lambda = d\left(\sin\theta_\mathrm{i} + \sin\theta_\mathrm{m}\right)\ , \tag{2.4}$$

where d is the line spacing of the grating, θ_i is the angle of the incident light and θ_m the angle of the diffracted light maxima, both relative to the normal of the grating, and m an integer describing the order of the constructive light interference. One can manually

choose a specific wavelength by varying the angle of incidence. The resolution of the radiation from the monochromators used at BESSY II depends on the photon energy but is typically about $10-100$ meV [32, 34], which is enough to selectively photoionize most inner-shell atomic orbitals [35–37]. In practice, the resolution is adjusted by using an exit slit, which also affects the light intensity. The radiation passing through the exit slit is guided toward the experimental chamber where it intersects a narrow plume of sample gas. The ionized particles from the sample gas are collected and recorded by using a *magnetic bottle spectrometer*, which is an efficient instrument for collecting as many charged particles as possible.

2.2 Magnetic bottle spectrometer

One way to measure the kinetic energies that particles receive in an ionization event is to measure the time it takes for them to travel a certain distance. Their velocities follow the simple formula

$$\text{velocity} = \text{distance/time} \ , \tag{2.5}$$

and, knowing the velocity, v, one can obtain the kinetic energy, ε, by the relation

$$\varepsilon = \frac{mv^2}{2} \ , \tag{2.6}$$

where m is the mass of the particle. There are many different types of electron *time-of-flight* (TOF) spectrometers and the designs are usually optimized for different purposes. The *magnetic bottle spectrometer* is an electron TOF spectrometer than can collect electrons emitted in essentially all directions from an interaction volume [39]. The magnetic bottle spectrometer can record electrons within a very large range of kinetic energies, which makes it a suitable choice when studying multi-electron ionization processes in atoms and molecules.

The principles of the magnetic bottle spectrometer used in this thesis are illustrated in Fig. 2.2. The spectrometer collects the electrons by relying on a strong divergent magnetic field in the interaction region. The strong field is generated by a ~ 1 T strong permanent neodymium iron magnet and shaped by a soft iron pole piece attached to the end of the permanent magnet. A weak axial magnetic field, which couples to the strong field, is produced by a solenoid current around the 2.2 m long flight tube. Figure 2.2 illustrates the partial field lines from both the strong and weak magnet (dashed gray lines) and how they couple to form the resulting field lines (solid gray lines). The Lorentz force

$$\vec{F} = q\left(\vec{E} + \vec{v} \times \vec{B}\right) \ , \tag{2.7}$$

generated by the magnetic field and a typically small electric field across the interaction volume, guides the electrons on a helical trajectory through the flight tube toward the electron detector located at the other end of the flight tube.

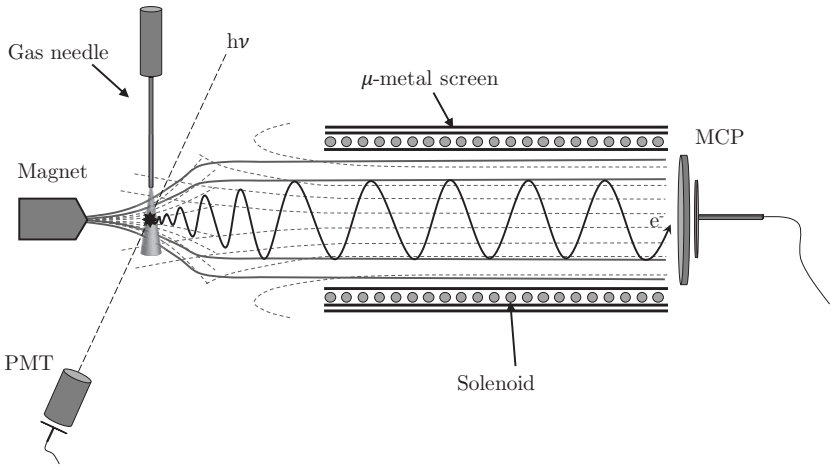

Figure 2.2: Schematic illustration of a magnetic bottle spectrometer.

2.2.1 Electron detector

The detector type used in the magnetic bottle instrument is a micro-channel plate (MCP) detector. The MCP detector is comprised of thin glass plates in which a large number of small channels are etched. The signal amplification principle of the MCP detector relies on an avalanching effect throughout the detector. A bunch of free electrons are emitted when a charged particle hits the surface of the channel walls. The electron bunch is accelerated by high electric fields through the plate structure toward the anode. The signal strength of the initial electron bunch is multiplied in a cascade fashion, as each new electron may collide with the walls and release new bunches of free electrons. The resulting voltage impulse at the anode is decoupled and the signal is fed to a discriminator. To enhance the sensitivity of the detector, multiple MCPs can be stacked so that adjacent channel-plates have an opposite rotation about the normal of the plate. The sensitivity of the detector is however never perfect and the detection efficiency typically ranges between $50-60\%$. Hence, about half of the particles that hit the detector surface will not be recorded. This can in certain cases lead to systematic problems, which will be discussed in section 2.3.2.2.

2.2.2 Time-to-energy conversion

The electron TOFs correspond to the time difference from the ionization event to when they hit the MCP. Since all electrons travel approximately the same distance within the flight tube, information about their flight times allows calculating the velocity and hence the kinetic energy of each recorded electron. The kinetic energies can be obtained

by using the equations

$$\mathrm{TOF} = \frac{d}{v} \ , \tag{2.8}$$

and

$$\varepsilon = \frac{m_e v^2}{2} + \varepsilon_0 \ . \tag{2.9}$$

Equation 2.8 relates the time it takes for an electron of velocity v, to travel the distance d, between the interaction region and the detector. The second equation relates the velocity and the mass of an electron, m_e, to kinetic energy. The term ε_0 is a correction term that accounts for additional energy gained or lost while moving through the spectrometer. This can relate to a manually set electric field or inhomogeneities caused by a small electrical charge-up in the spectrometer.

The reference signal is usually a signal from a photomultiplier that detects the light pulse. The TOFs are typically in the range of a few to thousands of nano-seconds, which is of the same order as electronic delays, t_{delay}, introduced by the acquisition system. The time elapsed from the ionization event until the reference signal and electron signals are recorded are, respectively

$$dt^{h\nu} = t^{h\nu}_{\mathrm{delay}} \ , \tag{2.10}$$

$$dt^{e^-} = \mathrm{TOF} + t^{e^-}_{\mathrm{delay}} \ . \tag{2.11}$$

The actual recorded quantity, t, relates to the true TOF according to

$$t = dt^{e} - dt^{h\nu} = \mathrm{TOF} + t_0 \tag{2.12}$$

where t_0 is the signal delay difference. One can combine Eq. 2.8, 2.9 and 2.12 to describe the kinetic energy in terms of the recorded time t, according to

$$\varepsilon = \frac{D^2}{(t - t_0)^2} + \varepsilon_0 \ , \tag{2.13}$$

where

$$D^2 = \frac{m_e}{2} d^2 \ . \tag{2.14}$$

As long as no experimental conditions are changed, one can treat D, t_0 and ε_0, as constant parameters that can be found by a proper calibration with a known spectrum. An example of the calibration procedure is given in Fig. 2.3. By recording time differences of electrons with known kinetic energies, one can use an optimization routine to solve for the most likely values of D, t_0 and ε_0. Once the fit parameters have been obtained, it is possible to map any t to corresponding kinetic energy ε, as shown by the red dashed line in Fig. 2.3.

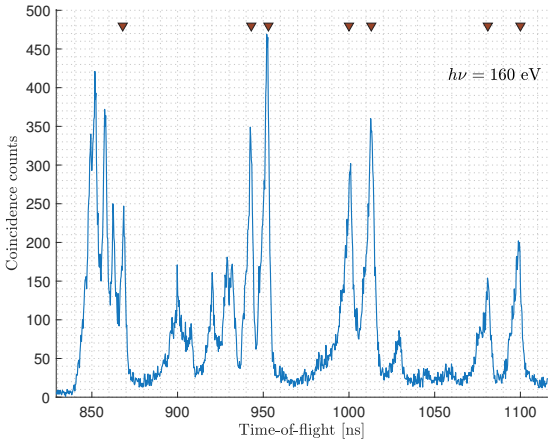

(a)

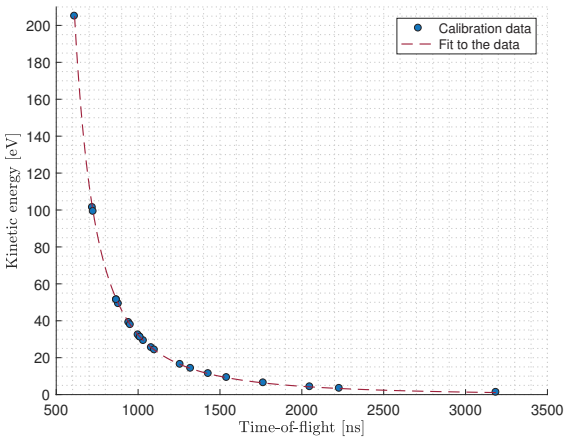

(b)

Figure 2.3: Example of the calibration procedure. a) Measured Auger spectrum of Kr used for calibration. The triangles denote a sample of chosen Auger lines used in the calibration. b) The interpolated dashed line represents the fit result after optimizing the D, t_0 and ε_0 parameters in Eq. 2.13 relative to the experimental data, represented by the blue dots.

2.3 Coincidence experiments

Coincidence experiments aim at detecting two or more particles that are correlated, which in our case means that they originate from the same ionization event. Coincidence TOF spectroscopy can be used to probe which particles are correlated and the kinetic energies they received in the ionization event. It is thus critical that the detected particles can be traced back to the same ionization event. A common method to ensure this is to use a pulsed light source and group signals from the particle detector that coincide with a specific light pulse. It is important that the pulse repetition rate is low enough that each particle has time to reach the detector before the next light pulse arrives.

The pulse repetition rate of a synchrotron is set by the bunch separation and the orbital frequency of the storage ring. The ring frequency of BESSY II is about 1.25 MHz, which translates to a detection window of about 800 ns. This is generally too short for the slowest electrons to travel all the way to the detector in a 2.2 m long magnetic bottle instrument, even when the storage ring operates in a single bunch mode. A high pulse repetition rate can thus lead to problems where slow electrons from one pulse are overtaken by fast electrons originating from a subsequent pulse. This will mix a real TOF spectra with so-called *ghost-lines*, which are real electrons but with shifted TOFs. One can usually identify the presence of ghost-lines by noticing equally intense copies of the same spectral line, separated in TOF by the characteristic ring period of the synchrotron. The ghost-lines can be removed completely, by reducing the pulse repetition rate. This can be achieved by using a *mechanical chopper*, which blocks some of the light pulses from entering the experimental chamber.

2.3.1 Mechanical chopper

The mechanical chopper used for this thesis was developed in 2012 by S. Plogmaker, a previous member of the research team [40]. It was designed specifically for the single bunch operation mode of BESSY II in Berlin. The chopper has two coaxial discs with two circular arrays of small slits that are evenly spaced. The outermost ring of arrays has 120 slits and the innermost ring has 15 slits. The two discs can be rotated relative to one another to set the opening time of the slits. The opening time must be less than the period between two consecutive light pulses to eliminate the risk of two light pulses passing through. The opening time for the BESSY II chopper is set to about 700 ns, which is about 100 ns less than the period of the storage ring.

The innermost array of slits can reduce the repetition rate to about 10 kHz and the typical repetition rate for the outermost ring is about 78 kHz. The 78 kHz repetition rate is well suited for electron only experiments. It is typically necessary to use the 10 kHz repetition rate for experiments involving ion detections, due to the longer flight

times of the ions. The chopper is also equipped with an electronic circuit that allows phase locking relative to a reference signal. The motor is driven by a frequency divided radio-frequency (RF) signal from the storage ring, and the phase locking feature adjusts for a potential drift of the motor signal relative to the RF signal. This ensures that the rotation of the disc is synchronized with the storage ring cycle so that the light intensity coming trough the slits is maximized.

2.3.2 False coincidences

The synchronized mechanical chopper is an effective solution for ensuring that no ghost lines are recorded. However, other features from unwanted coincidence detections can still appear in the recorded data. We call these features *false coincidences*. False coincidences are detections that appear as correlations but do not reflect physical correlations from the ionization process. There are several categories of false coincidences and it is important to understand how they are formed and how they may affect the data analysis. We will therefore mention the most common types and their implications.

2.3.2.1 Ionization of multiple species

There is always a risk that a single light pulse initiates more than one ionization event in the gas plume. Such event is referred to as *ionization of multiple species*. Ionization of two atoms or molecules may give rise to coincidence detections of electrons from two independent processes. False correlations, where e.g. an Auger line appears correlated with the wrong photoelectron line, can thus emerge in the analysis. The probability that a photon is absorbed by an atom or a molecule in the gas plume depends on the orbital cross sections, but also on experimental parameters, such as the light intensity and the gas pressure. Separate ionization processes can be considered independent and with a constant gas pressure and stable light intensity, the rate of ionization stays relatively constant over time. The probability that one light pulse initiates n independent ionization events can thus be described roughly using Poisson statistics. Using the average number of ionizations per light pulse, λ, one can model the probability using the Poisson distribution

$$P(n) = \frac{\lambda^n e^{-\lambda}}{n!} \ . \tag{2.15}$$

A good rule of thumb is thus to set the light intensity and gas pressure such that the rate of single ionization is about 1 in every 100 pulses. This can often be quickly evaluated using a simple rate meter and the repetition rate of the light source. For $\lambda = 0.01$, the probability of ionization of multiple species relative to a single ionization event is

$$\frac{P(n>1)}{P(1)} = \sum_{n=2}^{\infty} \frac{0.01^{(n-1)}}{n!} = 0.005 + \frac{0.01^2}{6} + \ldots \approx 0.00502 \ , \tag{2.16}$$

which is about 1 per every 200 single events.

2.3.2.2 Mixed coincidences

A combined collection-detection efficiency that is less than 100% may lead to mixed multi-detection data. This is important to consider in experiments where decay channels leading to multiple charge states are accessible. For instance, a triple ionization event, where only two of the released electrons were recorded, would appear as a two-electron coincidence detection. If the two detected electrons were released sequentially during a step-wise Auger decay, their energies may correspond to a 'true' intermediate state in the decay chain, although not the final state. In contrast, if the two detected electrons correspond to the first and third step in the decay chain, their total energy would add to represent a doubly ionized state that does not exist. In fact, the more particles that are produced, the higher the risk that the event is recorded falsely as an event involving fewer particles. The probability that an event producing n particles is recorded as a k-fold coincidence detection follows the binomial distribution, defined by the collection-detection efficiency f_e

$$B\left(k; n, f_e\right) = \sum_{n \geq k} \binom{n}{k} f_e^k \left(1 - f_e\right)^{n-k} \quad . \tag{2.17}$$

Figure 2.4 illustrates the probability distribution of detecting k-electrons in an $n = 5$-fold ionization event, given a 50% collection-detection probability per particle. The problem of *mixed coincidences* is difficult to circumvent and the best one can do is to maximize the collection-detection efficiency of the instrument. It is therefore important to be careful in the analysis and be alert to possible false coincidences.

2.3.2.3 Secondary ionization

A significant source of false coincidences are electrons that originate from surfaces in the experimental chamber. Fast photoelectrons or Auger electrons that manage to escape the confinement of the magnetic field lines can hit surfaces in the chamber and produce a cascade of *secondary ionization* of solid state electrons. These electrons can be caught by the magnetic field and travel toward the detector. It is often difficult to correct for secondary electrons in the data analysis, especially if they appear spectrally close to a real feature. The most efficient way to reduce the influence of secondary electrons is to identify the most likely surface source in the chamber and change the spectrometer conditions accordingly. It is therefore important to identify secondary electrons before recording the data. A high rate of secondary surface ionization typically relates to large components being close to the interaction region. This could be the magnetic pole piece, the gas needle or a heated oven source (sometimes used to sublimate a solid

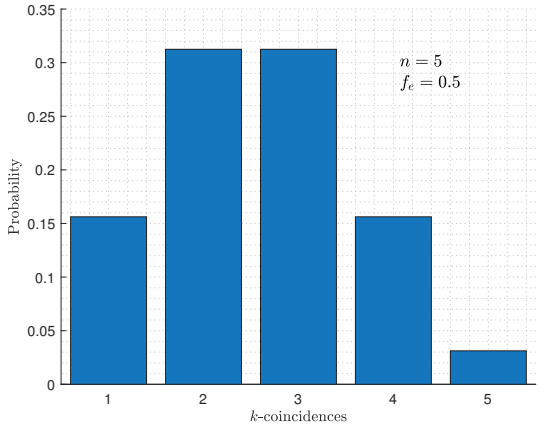

Figure 2.4: Bar diagram of the probabilities of detecting k electrons from a 5-fold ionization event. The probability is binomially distributed and defined here by a collection-detection efficiency of 50%.

sample into a gas). Surface ionization can lead to a shower of n secondary electrons, and the recorded k-fold secondary electron coincidences will also be binomially distributed. The simultaneous detection of real and secondary electrons may thus lead to mixed coincidences of more electrons than released in the *real* ionization process. For instance, a real double ionization event can be recorded as a false triple (or higher) ionization event, if one of the real electrons hits a surface and two (or more) secondary electrons are detected with the other real electron.

2.3.2.4 Accidental detection

Although the experimental chamber operates in high vacuum, there will always be stray background particles moving around in the chamber. The random walk of these stray particles allows them to sometimes hit the detector and be recorded by the acquisition system. Simultaneous detection of multiple stray particles, or detection of a single stray particle in coincidence with a real particle, causes another source of false coincidences. We refer to such false coincidences as *accidental detections*. As the stray particles are detected randomly in time, the associated noise signal can be approximated as uniformly distributed over all TOFs. A uniform TOF profile will be distributed non-uniformly in the corresponding kinetic energy domain as a consequence of the non-linearity in the TOF to kinetic energy conversion. This introduces an 'artificial' bias that leads to an enhanced relative background intensity of low kinetic energy noise compared to the high kinetic energy noise. One way to correct for this is to estimate the amount

of background noise in the TOF domain and simulate a uniformly distributed random sample of TOF data of equal size. The corresponding kinetic energies of the simulated data can then be subtracted from the experimental data in the kinetic energy domain.

2.3.3 Augmented VMI ion mass spectrometer

Electron data recorded in a coincidence experiment is important when analyzing ionization processes of molecules. However, all information regarding molecular relaxations can not be obtained by solely detecting electrons. It is important to also detect fragments from molecular dissociation to gain a complete picture of the processes.

The molecular orientations in an effusive gas plume are random by default. The spatial distribution of the fragments released in a dissociation process thus evolves statistically as an expanding sphere with time. The diameter of the sphere at any given time is set by the kinetic energy that the fragments received during the dissociation process. It is possible to measure both the mass-to-charge ratio and the diameter of such expanding spheres by applying an electric field that accelerates the particle spheres toward a position sensitive detector. The acceleration from the electric field will distort the geometry of the spheres in the direction toward the detector, but information about their diameters will be preserved in the tangential direction. The TOF and the diameter information of the projected spheres can be combined and used to infer both the mass-to-charge ratio of a detected particle and the kinetic energy it received from the dissociation. Coincidence measurements, targeting both electron kinetic energies and molecular fragments, can therefore be used to selectively study the full energy redistribution during a molecular relaxation process. This is a very powerful technique for studying the electronic processes underlying Coulomb explosions.

To employ this technique, we developed a versatile ion spectrometer that augments the magnetic bottle electron spectrometer. A schematic description of the latest electron-ion coincidence set-up developed by our team is presented in Fig. 2.5, with the ion spectrometer being the vertical component in the figure. The ion spectrometer relies on three hollow disc electrodes and a 0.5 m long flight tube. The electrode below the interaction volume is referred to as the *repeller*, the one above as the *extractor* and the top one as the *lens*. The holes in the center of the extractor and the lens are important to transmit the ions while the hole in the repeller plate is used to introduce sample gas into the interaction volume.

The ion spectrometer can operate in a TOF focusing mode, similar to a Wiley-Mclaren spectrometer [41]. However, by applying the right voltage ratios on the electrodes, the spectrometer can also operate under the *velocity map imaging* (VMI) principle [42]. The VMI principle has the advantage that particles with the same velocity vectors are focused to the same place on the detector, regardless of their origin in the interaction

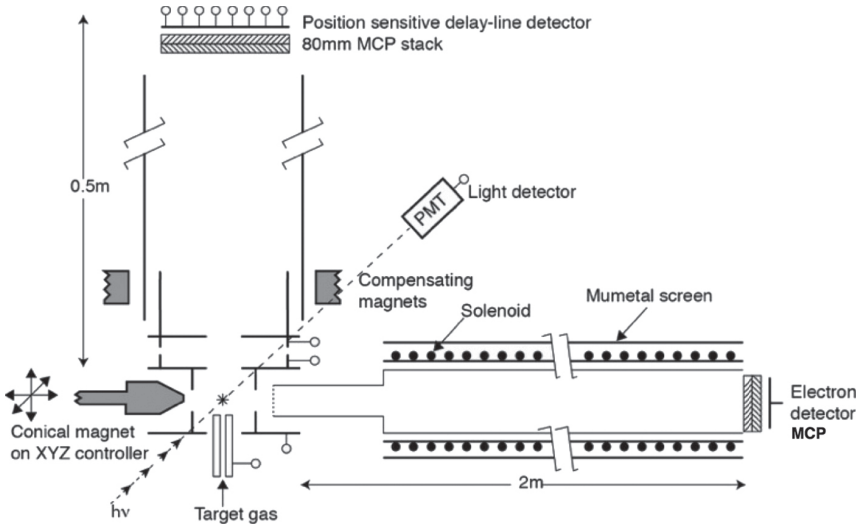

Figure 2.5: Schematic illustration of a magnetic bottle spectrometer augmented with a vertical ion VMI spectrometer [43].

volume. A VMI mass spectrometer that is combined with a position sensitive TOF detector can thus record more information from molecular fragmentations. The TOF and position data can be used to identify ions and obtain relative velocity components for each fragment in all three spatial dimensions. By combining the ion and electron information, one can backtrack how Auger decays and charge transfer processes break intermolecular bonds at different locations and angles within the molecule. This is a powerful but complicated technique and the spectrometer, while working properly, is undergoing further refinement.

2.4 Data analysis

A few of the important aspects to consider when analyzing data from coincidence experiments have already been mentioned in the preceding chapter. The discussions have so far considered technical aspects of the data acquisition and sources of noise that can affect the results negatively. This chapter will focus on the analysis of the acquired data, which aims to extract information about the physical processes under investigation. To this end, we start by considering a two-fold dataset of random variables $\mathbf{X}$ and $\mathbf{Y}$ that could describe e.g. spectra of kinetic energies. The covariance, which measures the strength of correlation between these two variables, is

$$\mathrm{Cov}\left(\mathbf{X},\mathbf{Y}\right) = \langle \mathbf{XY} \rangle - \langle \mathbf{X} \rangle \langle \mathbf{Y} \rangle \ . \tag{2.18}$$

The $\langle \mathbf{XY} \rangle$ term in Eq. 2.18 represents the average 2-dimensional histogram of the recorded events. When the ionization rate is very low, all particle detections are known to originate from the same ionization event, and the uncorrelated term $\langle \mathbf{X} \rangle \langle \mathbf{Y} \rangle$ becomes negligible. However, when the ionization rate is very high, ionization of multiple species per pulse will be likely. Particles emitted from multiple independent processes will thus often be recorded together and uncorrelated features, such as two strong Auger lines from two independent ionization processes, may appear strongly in the $\langle \mathbf{XY} \rangle$ term.

Data analysis of multi-particle detections can thus be separated into two categories, based on the importance of the uncorrelated term $\langle \mathbf{X} \rangle \langle \mathbf{Y} \rangle$. The first type of analysis is referred to as *coincidence analysis* and is applied to data where $\langle \mathbf{X} \rangle \langle \mathbf{Y} \rangle \approx 0$. The second category is referred to as *covariance analysis*, which is necessary when the term $\langle \mathbf{X} \rangle \langle \mathbf{Y} \rangle$ is no longer negligible.

2.4.1 Coincidence analysis

Coincidence analysis is the simplest and most straightforward way of analyzing multidimensional TOF data. The most common method of visual analysis is to form a so-called *coincidence map*. A coincidence map is a 2-dimensional histogram that is related to the first term in Eq. 2.18 [44] by

$$\mathrm{Coinc}\,(\mathbf{X}, \mathbf{Y}) = N_{\mathrm{events}} \langle \mathbf{XY} \rangle \ , \tag{2.19}$$

where N_{events} is the number of recorded ionization events. Coincidence mapping is an efficient method for identifying different types of decay correlations. To exemplify the use of coincidence maps, we show in Fig. 2.6 results from a simulated coincidence experiment of both direct and indirect ionization processes. The results are presented in two coincidence maps, where Fig. 2.6a represents correlations between two electron kinetic energies and Fig. 2.6b represents correlations between single electron kinetic energies and doubly ionized final states. For instance, direct and indirect decay steps can be identified by analyzing the features that these processes give rise to in the map. The kinetic energy of a photoelectron from a well defined atomic orbital is

$$\varepsilon_{\mathrm{photo}} = h\nu - E_{\mathrm{bind}} \ , \tag{2.20}$$

which corresponds to a discrete kinetic energy. Likewise, a well defined hole-state that decays by an indirect ionization process, such as an Auger decay, will lead to the release of an Auger electron with a discrete kinetic energy. A photoelectron detected in coincidence with an Auger electron will thus form a well defined island in a coincidence map.

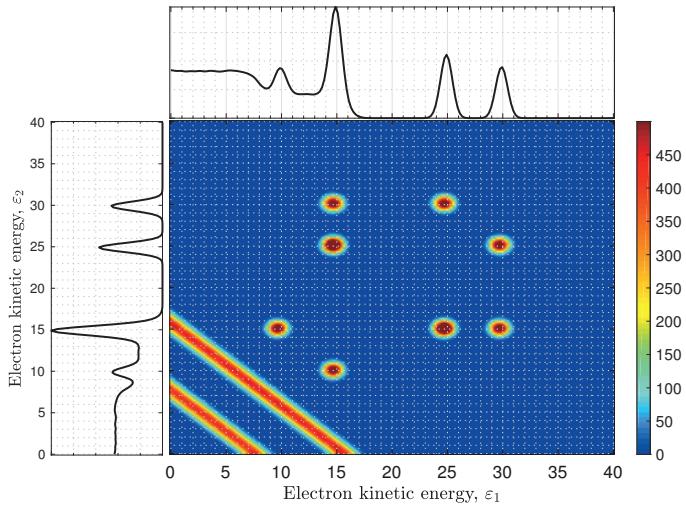

(a)

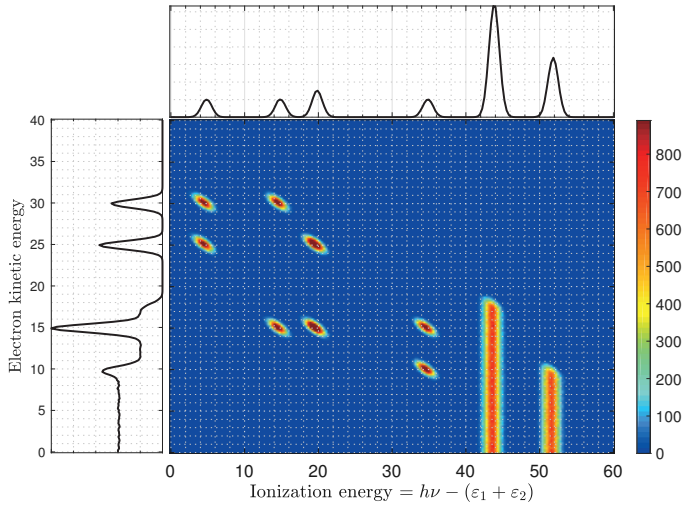

(b)

Figure 2.6: Simulated coincidence maps. Islands indicate indirect processes with discrete kinetic energies and continuous lines indicate direct processes where the excess energy is arbitrarily shared between the electrons. a) Correlations between two electrons. b) Individual electron kinetic energies (y-axis) correlated with different final states (x-axis).

In contrast, a direct double photoionization event is characterized by an arbitrary sharing of excess energy between the two released electrons. The total excess energy

$$E = \varepsilon_1 + \varepsilon_2 \ , \tag{2.21}$$

is constant, but the individual electron kinetic energies can range between $0 \leq \varepsilon \leq E$. In a coincidence map, this results in a continuous feature. In the kinetic energy domain, the continuous feature appears as a straight line, as seen in Fig. 2.6, and when plotting the map in the TOF domain, the same feature appears as a curved line.

Coincidence analysis of double particle detections can be extended to more than two particle detections ($k > 2$). A straightforward histogram would be k-dimensional and difficult to analyze. However, the analysis can be reduced to partial 2-dimensional maps. This can be exemplified by considering a dataset of three-fold particle detections, where each record corresponds to a detection of a single ion and two electrons. The relaxation processes that led to a given ionic state can be revealed in a 2-dimensional electron-electron coincidence map, by filtering the dataset on a selected ion. The filtering process is equivalent to selecting a 2-dimensional electron-electron map as a slice from the 3-dimensional ion-electron-electron histogram.

2.4.2 Covariance analysis

In experiments with a very high rate of ionization, traditional means of coincidence data analysis can to some extent break down. A typical example where such experimental conditions can be met is in low repetition rate free-electron laser (FEL) experiments, where the number of photons per pulse can be very high. The high number of photons in one light pulse can induce many ionization events across the gas plume. This leads to datasets with mixed information on correlated and uncorrelated processes. A traditional coincidence map of such data would thus be hard to interpret as all features would appear correlated with each other. To 'clean' a coincidence map from the uncorrelated electron events one can apply *covariance mapping* [44, 45].

Covariance mapping is based on the definition of the covariance of two random values but applied to two random vectors $\mathbf{X}$ and $\mathbf{Y}$. Every light pulse can be thought to as producing the two spectra $\mathbf{X}$ and $\mathbf{Y}$ with bins corresponding to the TOFs or kinetic energies. The covariance of bin X_i and Y_j is calculated according to

$$\Sigma_{ij} = \mathrm{Cov}(X_i, Y_j) = \langle X_i Y_j \rangle - \langle X_i \rangle \langle Y_j \rangle \ . \tag{2.22}$$

The first term in Eq. 2.22 corresponds to the average count in the ij:th pixel after N light pulses. The total covariance map is

$$\mathbf{\Sigma} = \begin{bmatrix} \Sigma_{11} & \Sigma_{12} & \Sigma_{13} & \dots & \Sigma_{1m} \\ \Sigma_{21} & \Sigma_{22} & \Sigma_{23} & \dots & \Sigma_{2m} \\ \vdots & \vdots & \vdots & \ddots & \vdots \\ \Sigma_{n1} & \Sigma_{n2} & \Sigma_{n3} & \dots & \Sigma_{nm} \end{bmatrix} , \tag{2.23}$$

which can be interpreted as a cleaned version of a traditional coincidence map after subtracting the expected number of uncorrelated counts in each bin.

The covariance analysis described above yields correct information when $\mathbf{X}$ and $\mathbf{Y}$ are only covariant with each other. A fluctuating parameter that affects the ionization rate, such as the light intensity, may also cause false structures in the map. If the ionization rate depends linearly on such a parameter, it is possible to subtract the contribution that is caused by this parameter. This is referred to as *partial covariance analysis* of a single fluctuating parameter [44, 46]. The partial covariance map can be obtained by

$$\mathrm{pCov}\left(\mathbf{X}, \mathbf{Y}\right) = \mathrm{Cov}\left(\mathbf{X}, \mathbf{Y}\right) - \frac{\mathrm{Cov}\left(\mathbf{X}, \mathbf{I}\right) \mathrm{Cov}\left(\mathbf{I}, \mathbf{Y}\right)}{\mathrm{Var}\left(\mathbf{I}\right)} , \tag{2.24}$$

where $\mathbf{I}$ is the fluctuating parameter. Figure 2.7 exemplifies each step in the partial covariance analysis of a simulated experiment of the same ionization processes as in Fig. 2.6, but with a much higher ionization rate and a light intensity that fluctuates between each pulse.

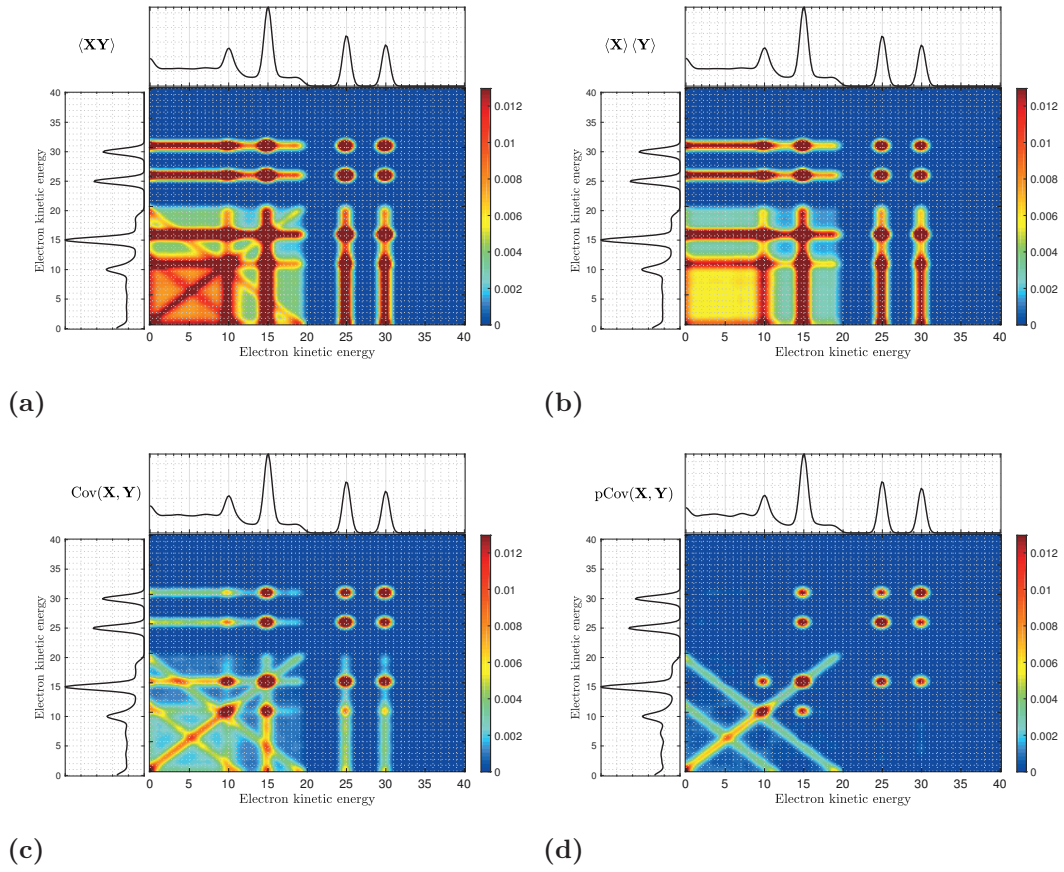

Figure 2.7: Simulated high rate experiment with a fluctuating light intensity of the same processes as in Fig. 2.6. a) Averaged raw data, b) partial map of the uncorrelated term, c) the covariance map and d) the partial covariance map.

Chapter 3

Results

The field of multi-coincidence studies on Auger cascades in atoms and molecules is still a fairly unexplored area of research. Considering the wealth of information on multi-electron processes that can be obtained from these studies, there is much that remains to be explored. In this thesis, we have studied multi-electron processes by relying on the experimental techniques described in the previous chapter. In particular, we have recorded coincidence data using a magnetic bottle spectrometer at the BESSY II synchrotron radiation facility in Berlin. The results from these studies are presented in full length in papers I-V. In the following sections, we will briefly describe the most important aspects and results from the studies, and discuss what the results mean for our understanding of relaxation processes in atoms and molecules.

3.1 Triple ionization of metal atoms

The combination of the high collection efficiency of a magnetic bottle spectrometer and tunable synchrotron radiation, serves well for coincidences studies on Auger cascades. A few multi-electron coincidence studies on different noble gases [47–51] and a few examples on metal atoms [52–55], based on similar techniques existed prior to this thesis. These previous studies demonstrated the efficiency of the technique and the amount of information that can be obtained on electronic relaxation. We have continued this exploration with two studies on multi-electron coincidences leading to triply ionized final states in atomic Cd and Hg. The results of these two studies are published in paper I and II. The most important aspects of these two articles will be discussed in the following two subsections.

3.1.1 Auger cascades of 4s and 4p inner-shell holes in atomic Cd

It has been shown that interesting correlation phenomena may occur in the inner-shell orbitals of atomic elements. Previous experiments have shown that a 4p vacancy in Xe is strongly associated with rapid $4p^{-1} \rightarrow 4d^{-2}$ super Coster-Kronig transitions, resulting in substantial broadening of spectral lines associated with the 4p vacancy [56]. Similar effects were also predicted for a 4p vacancy in Cd [13, 57] and were

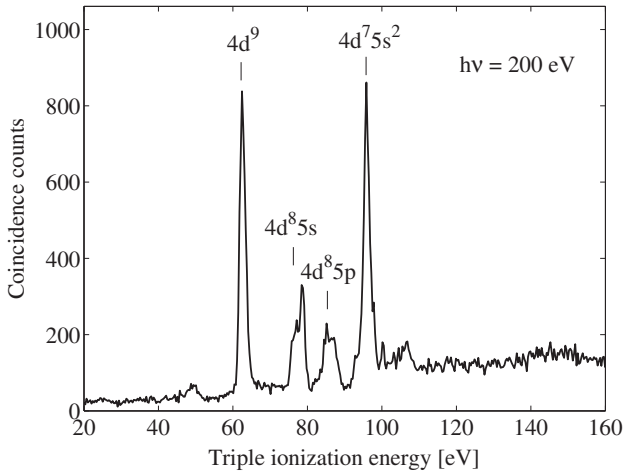

Figure 3.1: Experimental Auger cascade final state spectrum of Cd^{3+}, following the formation of single 4p or 4s vacancies using a photon energy of 200 eV.

subsequently observed in experiments [58]. The energy distribution between the two electrons associated with a 4p photoionization event, followed by a rapid $4p^{-1} \rightarrow 4d^{-2}$ transition, was observed directly in the study of double ionization of Cd [53]. This was possible due to the use of a coincidence detection technique, based on the same magnetic bottle spectrometer used in the experimental work of this thesis. The results showed that a 4p photoionization process was indeed strongly associated with a rapid decay to $4d^{-2}$ in Cd^{2+}, resulting in a significant broadening of the 4p photoelectron lines. The binding energy of the $4d^{-2}$ double hole state was found too low to allow further Auger decay to triply ionized states. However, the results from the study indicated that other double hole-states reached by 4s photoionization were energetically allowed to decay to Cd^{3+} [53].

In the study reported in paper I, we continued the spectroscopic exploration of Cd by studying Auger cascades leading to triply ionized final states. We used a photon energy of 200 eV, which is sufficiently high to allow photoionization of both the 4s and 4p orbitals in Cd. The ground state configuration of neutral Cd is

$$[Ar]3d^{10}4s^24p^64d^{10}5s^2,$$

which implies that there are three orbitals with lower binding energy than the 4s orbital and two orbitals with lower binding energy than the 4p orbitals. The experiment relied on three-fold electron detections, which allowed a more extensive study of the interesting behaviour of the orbitals in the N shell of Cd. The experimental data identified three final state configurations in Cd^{3+}, as shown in Fig. 3.1. The triple

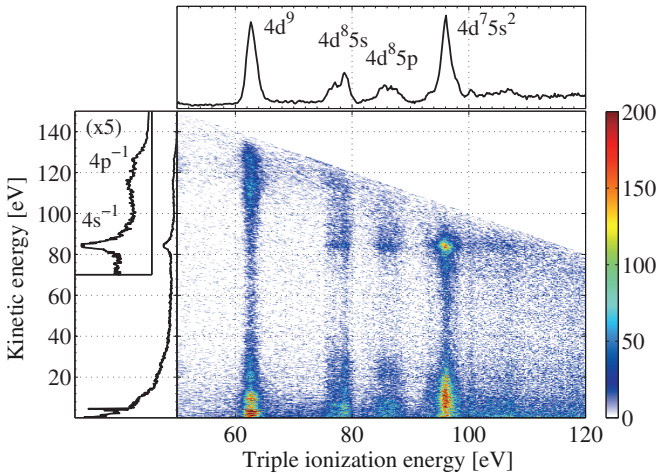

Figure 3.2: Coincidence map reflecting the formation of tricationic final states in Cd upon photoionization of a 4p or 4s electron using 200 eV photon energy. The triple ionization energy is on the horizontal axis and the single electron kinetic energies of the three detected electrons are on the vertical axis.

ionization energies (TIE) of the final states were determined using the measured kinetic energies of the three electrons involved in the formation of the final states, according to the energy relation

$$\mathrm{TIE} = h\nu - (\varepsilon_1 + \varepsilon_2 + \varepsilon_3) \ , \tag{3.1}$$

where ε denotes a single electron kinetic energy. The experimental results were interpreted with aid of multiconfigurational Dirac-Fock (MCDF) computations [59, 60], which allowed identification of the final state peaks. The three-fold coincidence data were analyzed by mapping the single-electron kinetic energies involved in the production of each final state in a coincidence map shown in Fig. 3.2. The correlations shown in the map indicated that the ground state configuration in Cd^{3+} was strongly associated with broad features of kinetic energies close to what would be expected from 4p photoelectrons. The broad features at low kinetic energies also resembled the expected results from rapid $4p^{-1} \rightarrow 4d^{-2}$ decays. However, as the binding energy of the $4d^{-2}$ configuration in Cd^{2+} was shown to be lower than the ground state energy of Cd^{3+} [2, 53], it implied that other processes are involved.

To identify these processes, we extended the computations to include monopole shake-up processes in both the photoionization step and in the super Coster-Kronig decay of the 4p vacancy. Since the first step in the cascade involved a 4p vacancy, the corresponding Auger spectrum showed very broad features. However, the experimental spectrum of the second Auger decay step showed distinct Auger lines of low kinetic

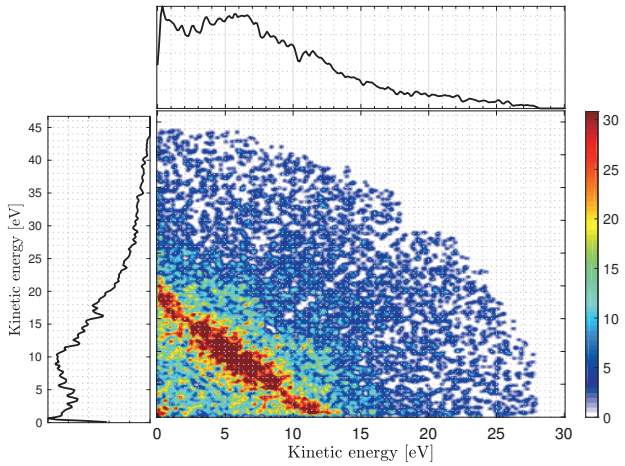

Figure 3.3: A coincidence map of Cd reflecting the kinetic energy correlations of the two Coster-Kronig electrons released in the decay channel described by Eq. 3.2, leading to the $4d^{-3}$ final state configuration in Cd^{3+}.

energy that could be compared with the numerical results. The comparison showed good agreement between the experimental and theoretical results and the Auger decay channels leading to the ground state of Cd^{3+} could thus be identified.

The experimental results presented in Fig. 3.2 showed that the $4d^7 5s^2$ states in Cd^{3+} were associated with a 4s photoelectron and broad features of low kinetic energies. The results from the computations, and from the previous study on Cd^{2+} [53], both suggested that the decay of a 4s vacancy is associated with the $4p^{-1}4d^{-1}$ configuration in Cd^{2+}. The $4p^{-1}4d^{-1}$ states have been speculated to be very short lived as well, due to rapid $4p^{-1}4d^{-1} \rightarrow 4d^{-3}$ super Coster-Kronig decays [58, 61], resulting in strong broadening effects in the corresponding Auger spectra. Auger decay channels from a 4s vacancy to the $4d^7 5s^2$ states in Cd^{3+}, via the intermediate $4p^{-1}4d^{-1}$ configuration, thus involve a 4p vacancy in both steps of the decay channel

$$4s^{-1} \rightarrow 4p^{-1}4d^{-1} \rightarrow 4d^{-3} \ . \tag{3.2}$$

The experimentally measured kinetic energies of the two electrons detected in coincidence with the 4s photoelectrons are plotted in a coincidence map, shown in Figure 3.3. The map shows a continuous energy distribution between the two electrons, which suggests that the decays are very fast. The experimental results agree with the anticipated behaviour of two rapid super Coster-Kronig decays involving a 4p vacancy. However, the distribution also resembles an energy sharing distribution expected from a direct

$4s^{-1} \rightarrow 4d^{-3}$ double Auger decay. The observed process constitutes an interesting example where the distinction between a very rapid step-wise decay and a direct double Auger decay becomes rather ambiguous.

3.1.2 Auger cascades of 4d inner-shell holes in atomic Hg

Studies on Auger cascades leading to triple ionization of atomic Hg had prior to this thesis been performed for decays of vacancies down to the 4f orbital [52, 54, 55]. In paper II, we present results from a new spectroscopic investigation of triply ionized states in Hg, produced by photoionization of 4d electrons. The study relied on the same experimental set-up and three-fold electron coincidence detection technique as in the study on Cd, in paper I, which allowed a complete study of the $4d^{-1}$ Auger cascades leading to states in Hg^{3+}. The experiment was performed at beamline U49/2-PGM-2 at BESSY II using a photon energy of 730 eV for the 4d photoionization. Previous spectroscopic studies on single Auger decay in Hg had, along with theoretical studies, shown that the decay branching of the $4d^{-1}$ vacancy was significantly influenced by

$$4d^{-1} \rightarrow 4f^{-1}(nl)^{-1} \tag{3.3}$$

Coster-Kronig transitions [62]. Our coincidence detection technique allowed us to study these processes further by analyzing the Coster-Kronig electrons detected in coincidence with 4d photoelectrons. Furthermore, the three-fold detection scheme allowed us to analyze the Auger electrons emitted from the subsequent decay of the $4f^{-1}(nl)^{-1}$ states. As three sequentially emitted electrons were recorded together, a triple ionization spectrum could be formed. This final state spectrum is shown in the top panel of the coincidence map presented in Fig. 3.4. The map displays the individual electron kinetic energies of the two Auger electrons involved in the formation of each peak in the final state spectrum. The experimental data revealed that the decay channels leading to the five observed final state peaks all involved a $4d^{-1} \rightarrow 4f^{-1}(nl)^{-1}$ Coster-Kronig decay in the first step.

Prior to our study, two independent studies had shown contradictory experimental results on the branching ratio for these decay channels [62, 63]. To shed new light on this issue, we compared our experimental results with theoretical values obtained by MCDF calculations. By selecting the Coster-Kronig spectrum detected in coincidence with a $4d^{-1}$ photoelectrons, we could deduce the branching ratios of the $4d^{-1} \rightarrow 4f^{-1}(nl)^{-1}$ decay in a way that significantly reduced the level of background noise compared to the previous studies. We found good agreement of our experimental and theoretical results as well as the results from one of the two previous studies [63].

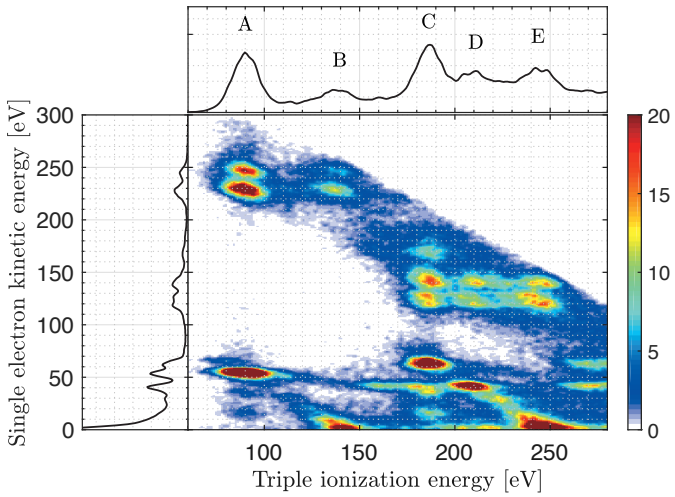

Figure 3.4: Coincidence map representing the formation of states in Hg^{3+} upon photoionization of 4d electrons using 730 eV photon energy. The triple ionization energy is on the horizontal axis and the single electron kinetic energies of the two Auger electrons are on the vertical axis. The denotations A-E refer to the final state regions described in Fig. 3.5.

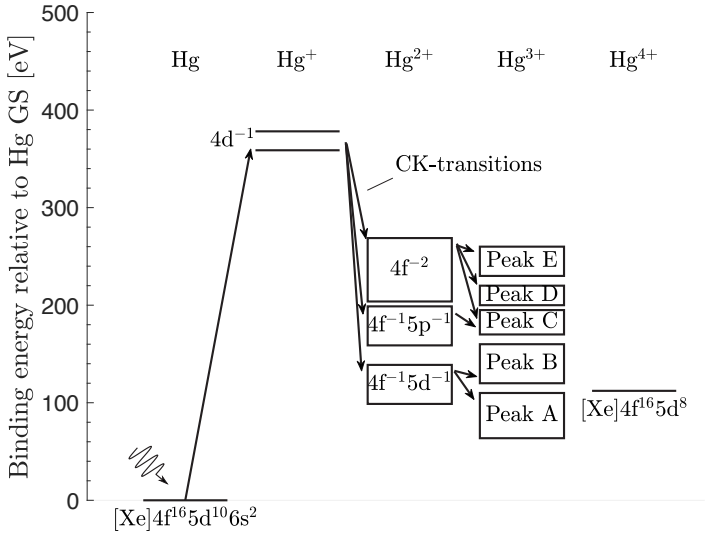

Figure 3.5: Energy-level diagram of atomic Hg for different charge states. The arrows indicate possible transition channels leading to the first three charge states.

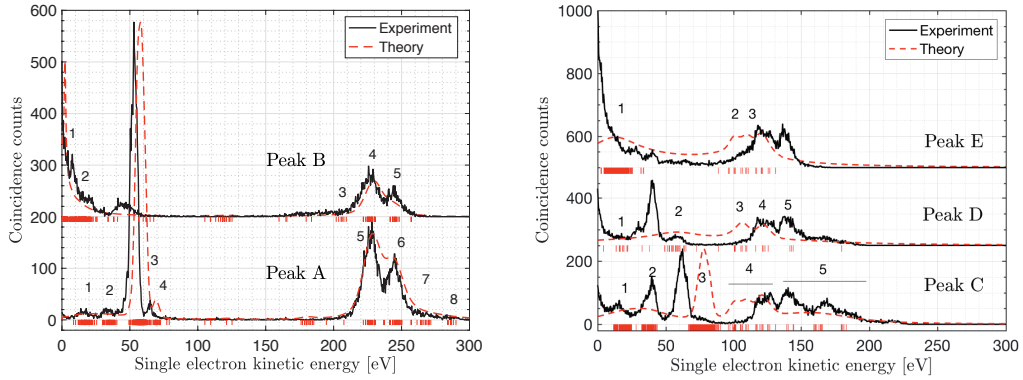

Figure 3.6: Single Auger electron spectra of the last decay step leading to the observed final state peaks in Hg^{3+}.

The $4f^{-1}(nl)^{-1}$ states are energetically allowed to decay to triply ionized states by another Auger decay, as shown in Fig. 3.5. Final state candidates for the peaks labelled A-E in the spectrum shown in the top panel of Fig. 3.4, were identified with aid of MCDF calculations. By comparing experimental and theoretical single electron spectra of the last Auger decay step, we could assign the most likely channels for this step as well. An experimental and theoretical comparison for the last decay step can be seen in Fig. 3.6. The states above the Hg^{4+} threshold are expected to decay again and the observed states correspond in this case to a snap-shot in a decay chain that continues to higher charge states. This introduces both an uncertainty in the theoretical computation of Auger transition rates and the risk of mixed coincidences that may result in false features in a coincidence map. We found good agreement between theory and experiment for the two final state peaks A and B. We could also conclude that final state peaks C and E were likely real, and could suggest the most likely configurations for these states. The interpretation of peak D was more complicated and we could not rule out it being formed by false coincidences.

Auger cascades such as those studied in paper I and II involve comparatively deep lying inner shells. Experimental studies of these processes are important, not only for testing our models of these atoms, but also because the processes are believed to significantly influence the nature of Coulomb explosions in molecules containing similar atoms. Molecular bonding involves primarily valence electrons, which means that deeper inner-shell electrons often behave relatively atomic-like, even in molecular species. Auger cascades in molecules containing Cd or Hg, initiated by an atomic-like inner-shell vacancy localized at these atoms, are thus expected to branch in a similar way to the decays studied in these atoms. The observed decay channels hence

reveal important information on how the vacancies accrue and propagate upward in the energy level structure. The relative branching at each step of the process can thus disclose which bonds are likely to be broken, and in which order, when the vacancies enter the bonding orbitals. This is important for understanding the charge-build up that underlies Coulomb explosion of molecules and radiation damage. However, detection of all electrons emitted by Auger cascades leading to very high charge states can quickly become too complex to be practically achievable. The total charge produced by an inner-shell vacancy can however be studied by detecting the ions produced from such events. In the next section, we will discuss results on an experimental study on the formation of different ionic charge states upon formation of selective inner-shell vacancies.

3.2 Charge state branching of Auger cascades in Xe

A step-wise Auger cascade can be described as a complex relaxation network between an initial hole-state and hole-states of increasing degree of ionization. The number of pathways in the network increases rapidly the deeper the initial hole-state lies. A complete relaxation network, including all possible states and transitions, can thus be highly complex for deep orbital vacancies in many-electron systems. To gain a better understanding of the mechanisms driving Coulomb explosions and various types of radiation damage, it is nevertheless important to develop and test models that predict the final results of Auger cascade networks. One such result is the charge production, which is an important factor that drives the dynamics of Coulomb explosions.

With the new ion-electron coincidence set-up, described in Ch. 2.3.3, we gained the additional capability to detect ions and selectively filter the charge states produced from photoionization of specific orbitals. The set-up combines the qualities of the magnetic bottle spectrometer with the ability to detect ion mass spectra in coincidence with the electrons. The new instrument was used for the first time in the study in paper III, where we measured the distribution of Xe^{n+} charge states produced from photoionization of 3p, 3d, 4s, 4p and 4d electrons. The decay branching to different Xe^{n+} charge states were experimentally estimated and the results are summarized in Table. 3.1, and compared with theoretical predictions in Fig. 3.7. The results show that the most likely produced charge state increases with the binding energy of the initial hole-state. This agrees with the step-wise decay model, where the decays favour orbitals that are spatially close, as long as the relaxation in energy is enough to release an Auger electron. The relative difference in binding energy of two adjacent nl and $(n+1)l'$ orbitals increases deeper down in the orbital structure, making the energy

Table 3.1: Experimentally determined charge state branching ratios from photoionization of different subshells in Xe.

	$4d_{5/2}$	$4d_{3/2}$	'4p'	4s	3d	$3p_{3/2}$	$3p_{1/2}$
Xe^{2+}	83.7 ± 1	79.5 ± 1	3 ± 1.5				
Xe^{3+}	16.3 ± 1	20.5 ± 1	62 ± 3	34 ± 10	$4.7 \pm .2$		
Xe^{4+}			35 ± 7	35 ± 8	53.7 ± 1	$3 \pm .8$	3.2 ± 1.5
Xe^{5+}				30 ± 5	25.6 ± 1	$16.8 \pm .8$	9.1 ± 2.2
Xe^{6+}					13 ± 4	28.3 ± 2	27.2 ± 3.3
Xe^{7+}					2.4 ± 3	38.6 ± 3.6	39.6 ± 3.6
Xe^{8+}					$0.4 \pm .2$	11.5 ± 1.5	16.4 ± 2.4
Xe^{9+}						$1.7 \pm .6$	4.5 ± 1

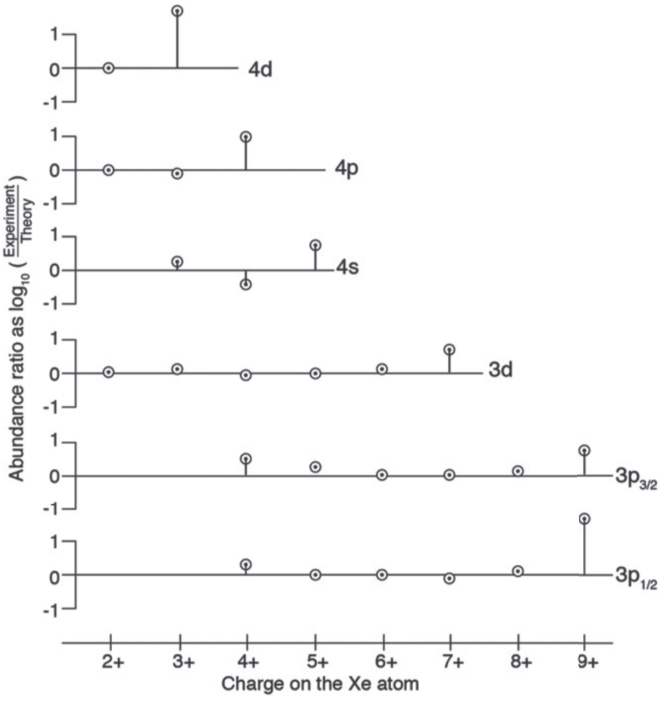

Figure 3.7: Comparison of experimental and theoretical charge state abundance from the decay of measured hole-states of Xe.

requirement more likely to be fulfilled the deeper the initial vacancy. A step-wise relaxation of the initial hole-state leads to a distribution of charge states, statistically weighted by the number of pathways leading to each charge state.

A subset of the results in Tab. 3.1 are presented in bar diagrams in Fig. 3.8. The forms of the distributions shown in Fig. 3.8 resemble probability distributions characterized by combinatorial rules, suggesting the number of pathways to be the driving factor for the overall shapes of the charge state distributions. For instance, in Fig. 3.8, we compare the measured total charge state distributions with zeroth-order approximations based on the hypergeometric distribution, represented as red dashed curves. The hypergeometric distributions describe the probability of randomly distributing a given number of holes in orbitals that may or may not allow further Auger decay. We can see that the overall shapes agree reasonably well with the experimental results. However, the probability of producing Xe^{4+} in Fig. 3.8a deviates strongly from the overall shape, which suggests that some channels in the decay chain might be so strong that they cause a bias toward producing Xe^{4+} and effectively 'remove' other degrees of freedom in the network. This could potentially be due to Coster-Kronig transitions in the N-shell, which are known to strongly affect the relaxation network [48].

Xenon is a prototype atom that can be used as a model for related elements that are often found in molecules. Iodine ($Z = 53$) is next to Xe ($Z = 54$) in the periodic table but is, in contrast to Xe, a chemically active element. Molecules containing I are often used as prototypes in studies on Coulomb explosion. The results on atomic Xe may therefore function as a model for the behaviour of I in Coulomb explosion of molecules, such as CH_3I [64] or ICN, initiated by a vacancy in a deep subshell of I. In the next section, we will test this hypothesis and further discuss the results on Coulomb explosion of ICN.

3.3 Coulomb explosion of ICN

The study on charge-state resolved branching ratios in Xe gives important information on how Auger cascades may progress in atoms similar to Xe. As the next step in the study of Auger cascades, we turned to the iodine based molecule ICN. The results from this study formed paper IV, where we studied Coulomb explosion as a result of selective inner-shell ionization of iodine. The experiments were based on the magnetic bottle spectrometer with the augmented ion spectrometer operated in VMI conditions.

The study was an extensive investigation of the fragmentation patterns at several different photon energies. The multi-electron, multi-ion coincidence technique allowed filtering mass spectra by selecting on both photoelectrons and Auger electrons. We studied the fragmentation patterns separately for photoionization of I 4d, I 4p, I 4s,

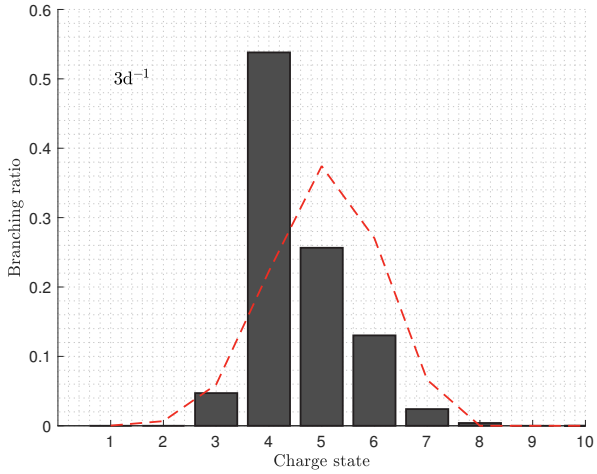

(a)

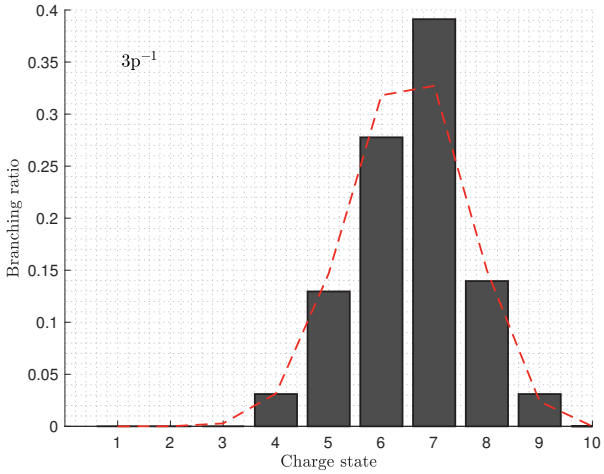

(b)

Figure 3.8: Total charge state distributions from orbital relaxations. The bar diagrams represent experimentally measured ratios and the dashed red curves correspond to hypergeometric distributions. The subplots correspond to the relative charge production upon photoionization from the a) 3d orbital or b) 3p orbital. The results in panel a) and b) resemble hypergeometric distributions, with some biases toward particular charge states.

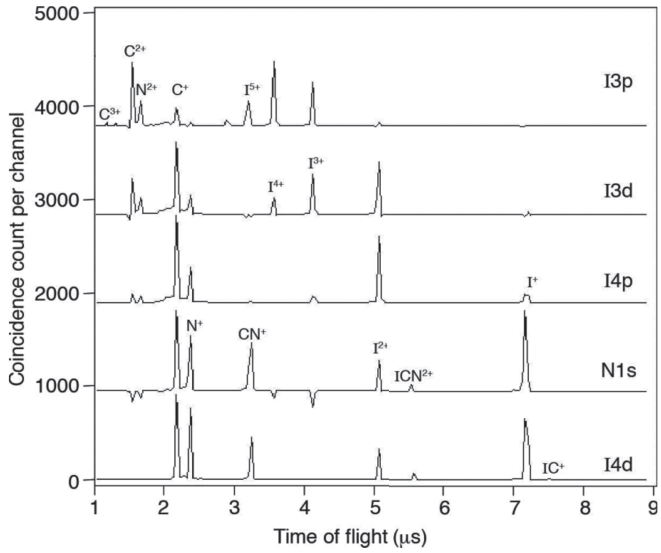

Figure 3.9: Mass spectra from fragmented ICN recorded in coincidence with different photoelectrons at different photon energies. Background and accidental coincidences have been subtracted. The hollowness of the light ion features are due to instrumental inefficiency in detecting all emitted fragments.

C 1s, N 1s, I 3d and I 3p, and experimentally measured the molecular binding energies of these orbitals by scanning the photon energy across the threshold region. By filtering the coincidence data on events involving a specific photoelectron, we could obtain total mass spectra for the Coulomb explosion of each initial hole-state. A selection of the measured mass spectra is shown in Fig. 3.9.

Some systematic trends that we observed from these experiments were, as in the case of Xe, that the degree of ionization increases as deeper shells are vacated. We could also confirm that molecular fragments are less likely to be observed with higher ionized atomic fragments. The molecular fragments abruptly disappeared from the mass spectra as more highly charged iodine ions were formed. The results in Fig. 3.9, show that the CN ions disappear when probing the I 4p or deeper orbitals. At the same time, iodine ions with charges greater than 2 start to appear. This suggests a step-wise Auger cascade, where the first steps in the decay chain involve localized atomic-like iodine orbitals. As the degree of positive charge sequentially builds up, the vacancies move upward in the energy level structure to eventually enter molecular orbitals, where bond breaking and charge transfer effects are likely.

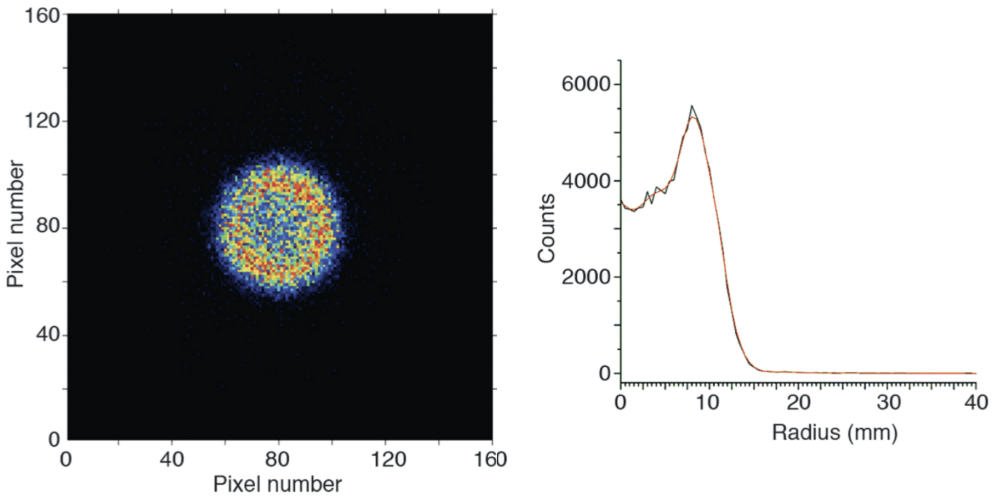

Figure 3.10: Left panel: Velocity map image of I^+ fragments recorded in coincidence with I $4d_{5/2}$ photoelectrons, at 110 eV photon energy. Right panel: radial intensity distribution.

The most probable total degree of ionization upon the removal of an I 4p electron was found to be four-fold with three-fold ionization being the second most likely result. Photoionization of I 3d was found to lead to three- to seven-fold ionization, with the first and second most likely degree of ionization being 4 and 5 respectively. The total degree of ionization from photoionization of I 3p were found to range between four- to nine-fold with the most abundant charge states being 6 and 7. These degrees of ionization agree well with the measured charge state distributions of the related orbitals in Xe. This is an interesting result that agrees with the hypothesis that the progression of Auger cascades in molecules, initiated in deep inner-shells of heavy atoms occur primarily step-wise in an atomic-like fashion until vacancies involve orbitals of molecular character.

Finally, the study in paper IV successfully demonstrated that the newly developed ion spectrometer could operate as a multi-electron, multi-ion coincidence instrument with VMI capability for the ion detections. By employing the VMI principle, the Coulomb explosion kinetic energy release of singly and doubly charged iodine ions recorded in coincidence with I $4d_{5/2}$ and I 4p electrons could be obtained. Figure 3.10 shows the recorded I^+ image coincident with an I $4d_{5/2}$ photoelectron. The radii of the observed rings relate to the kinetic energy of the fragments and can be used to derive the total kinetic energy release of a Coulomb explosion.

3.4 Energy sharing in direct double photoionization of He

In contrast to large parts of the previous discussion, the study in paper V investigated processes in which two electrons are emitted directly from an atomic system, without involving a step-wise decay. We have seen how very rapid Coster-Kronig decays can result in a continuous energy sharing between electrons and challenge viewing some Auger decays as step-wise processes. Direct double photoionization and direct double Auger decay are two other processes in which two electrons share the available excess energy in a continuous fashion. The study in paper V, focused on how the two electrons share the available excess energy in single-photon direct double photoionization of He. The question was approached with the aim to effectively parametrize and build an empirical model for the energy sharing distributions, and to describe their dependence on the available excess energy. The objective of having a model for direct double photoionization of He is to effectively compare similar processes in other systems to gain a better insight on the systematics of direct processes.

To this end, we measured energy sharing distributions by collecting both electrons released in the single-photon direct double ionization process and recording their kinetic energies. The electron pairs, involved in the formation of He^{2+}, could be identified by their total kinetic energy sum, as the double ionization potential follows

$$\mathrm{DIP} = h\nu - (\varepsilon_1 + \varepsilon_2) \ . \tag{3.4}$$

The energy sharing distributions from direct double photoionization of He are known to gradually turn from flat to $\cup-$shaped as the excess energy increases [20, 23–25]. This can be seen in Fig. 3.11, which presents a sample of the measured distributions. Energy sharing distributions were recorded for a number of excess energies, ranging between $11 - 221$ eV, to systematically study the gradual transformation of the distributions from being flat to $\cup-$shaped. The measured energy sharing distributions were modelled efficiently by fitting the empirical model

$$\hat{S}\left(\varepsilon; E\right) \sim e^{f(E)\frac{\varepsilon}{E}\left(1-\frac{\varepsilon}{E}\right)} \ , \tag{3.5}$$

to the experimental data. Here, f represents an unknown function that sets the shape of the distribution, E the total excess energy and ε the electron kinetic energy. The total energy sharing distributions can, as mentioned in Ch. 1, be modelled by [24, 25]

$$S_{\mathrm{tot}}(\varepsilon; E) = \left|a_{f,i}^{\mathrm{KO}}\right|^2 + \left|a_{f,i}^{\mathrm{SO}}\right|^2 + C_{\mathrm{int}} \ , \tag{3.6}$$

where $a_{f,i}^{\mathrm{KO}}$ and $a_{f,i}^{\mathrm{SO}}$ are the transition amplitudes for the SO and KO mechanisms, respectively. As the interference term was found negligible for He [25], the total sharing distribution curves reduce to a sum of the two separate KO and SO distributions

$$S_{\mathrm{tot}}(\varepsilon; E) = S_{\mathrm{KO}}(\varepsilon; E) + S_{\mathrm{SO}}(\varepsilon; E) \ . \tag{3.7}$$

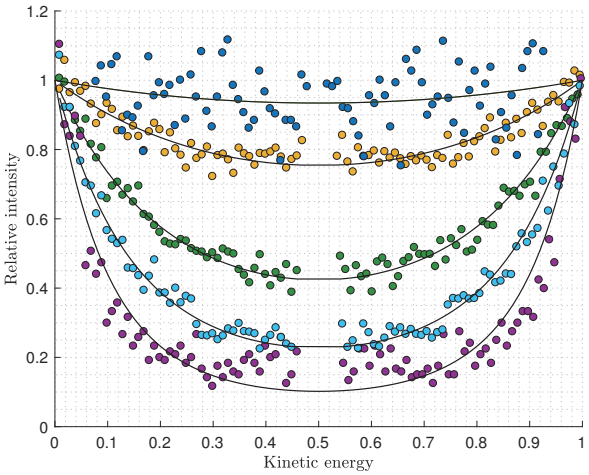

Figure 3.11: Energy sharing distributions measured at five different excess energies. The curves are, descending vertically in the plot, the distributions obtained at excess energy 11, 51, 101, 161 and 221 eV, respectively.

Extracted estimates of $S_{\mathrm{KO}}(\varepsilon; E)$ were obtained by subtracting theoretical $S_{\mathrm{SO}}(\varepsilon; E)$ distributions from the experimental measured $S_{\mathrm{tot}}(\varepsilon; E)$ distributions. An example of the procedure is shown in Fig. 3.12. The blue dots represent the measured $S_{\mathrm{tot}}(\varepsilon; E)$ distribution and the red line the calculated $S_{\mathrm{SO}}(\varepsilon; E)$ distribution. The estimated $S_{\mathrm{KO}}(\varepsilon; E)$ distribution, obtained by subtracting the red SO curve from the blue dots, is represented with green dots. This procedure resulted in three separate energy sharing distributions, one for the total, a second for the KO and a third for the SO mechanism, for each excess energy.

The function $f\,(E)$ in Eq. 3.5 was treated as a fit parameter to be optimized for each distribution and excess energy. The values obtained for the shape functions $f\,(E)$ for the total, KO and SO distributions are shown in Fig. 3.13. The shape function shows a linear trend that goes through the origin for all three distributions, which in this case suggests that $f(E)$ can be substituted by

$$f(E) = kE \ , \tag{3.8}$$

with k being a single parameter that defines the shape of each distribution. The estimated $k-$parameters for the three distributions are presented in Table 3.2 and compared with corresponding values obtained from theoretical distributions, simulated by Schneider et. al. [24, 25]. The total and KO distributions from the experimental data agree fairly well with the corresponding theoretical distributions. This suggests that

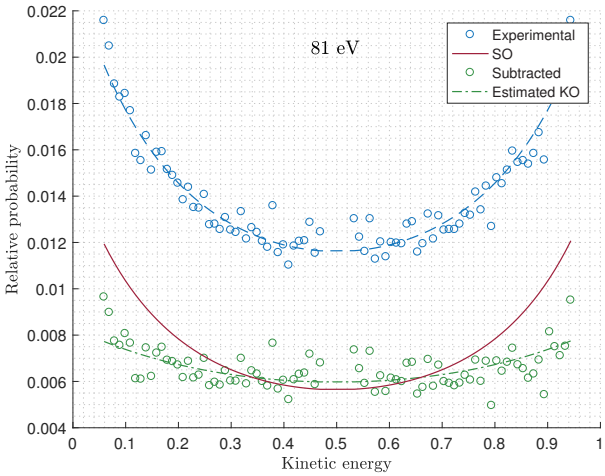

Figure 3.12: Energy sharing distributions at $E = 81$ eV. The blue dashed line shows the model fit to the blue dots representing the experimentally measured total sharing distribution. The solid red line represents the calculated SO contribution and the green dot-dashed curve represents the fitted KO distribution, obtained by subtracting the SO part from the total experimental distribution.

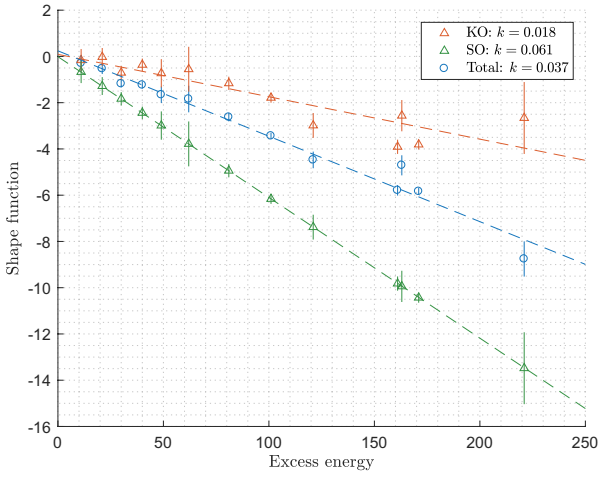

Figure 3.13: Linear fit through the optimized shape function value at each excess energy.

Table 3.2: Estimated values for the shape parameter k from simulations, k_{theory} [24, 25] and experimental distributions, k_{exp}, along with the associated 95% confidence intervals, including the uncertainty in the model fitting.

	Knock-out	Shake-off	Total
k_{theory}	0.029	0.061	0.038
c.i(k_{theory})	(0.028, 0.030)	(0.057, 0.065)	(0.032, 0.043)
k_{exp}	0.022	-	0.036
c.i(k_{exp})	(0.018, 0.026)	-	(0.033, 0.039)

the separation of KO and SO is justified, not only from the perspective of the direct double photoionization cross section, but also for the corresponding energy sharing distributions.

The results in paper V form an interesting starting point for testing the KO and SO separation of similar processes in other systems. The method to parametrize the energy sharing distributions is not limited to the case of He, and we hope that it can prove useful when studying other direct processes, such as direct double photoionization and direct double Auger decay in other atomic and molecular systems.

Chapter 4

Summary

The studies on Auger cascades in atomic Cd and Hg in papers I and II demonstrate the wealth of information that can be obtained from studying electron coincidences. The coincidence detection scheme used in these experiments offers many options in the data analysis. Both studies demonstrate how each step in an Auger cascade can be singled out and analyzed separately, which makes comparison with simulated spectra possible for each step in the decay chain. This is important for understanding the finer details of a complete relaxation network and for understanding the final outputs, such as the produced charge state distributions. In both papers I and II, we compared experimental and theoretical single electron spectra of specific decay steps. These comparisons found interesting agreements with theory but highlighted also important parts which need further investigation. The study in paper I highlighted the importance of including shake-up transitions, both in the photoionization step and the Auger decay steps, to explain the decay channels leading to the $4d^9$ ground state configuration of Cd^{3+}. The experimental data from the Auger cascade leading to the $4d^75s^2$ states could confirm that the decay chain $4s^{-1} \rightarrow 4p^{-1}4d^{-1} \rightarrow 4d^{-3}$ is the strongest channel and results in rapid Coster-Kronig decays with large broadening of the Auger lines. The short lifetimes broaden the distribution of kinetic energies to the extent that it covers the entire span between the binding energies of the $4s^{-1}$ and $4d^{-3}$ states. The experiments found that the two emitted electrons share the available energy in a continuous fashion, similar to a direct double Auger decay.

The importance of Coster-Kronig decays were also demonstrated in the study on Hg in paper II. We could confirm the previous reports that a $4d^{-1}$ vacancy decays almost exclusively by Coster-Kronig transitions to $4f^{-1}$ $(nl)^{-1}$ states. The high degree of selectivity, offered by using a coincidence detection technique, allowed us to resolve the conflicting results on the Coster-Kronig branching ratios by eliminating the influence of undesired background contributions. Accurate branching ratios for the Coster-Kronig decays are important as these decays so strongly characterize the Auger cascades passing through the affected intermediate states. Strong Coster-Kronig transitions define local features of the relaxation network, and insufficiently accurate branching ratios may thus result in inaccurate predictions of the final outputs, such as the produced charge states.

The charge state distributions produced by photoionization of different subshells in Xe were measured in paper III. This study showed that both the highest, and most frequently produced final charge state, increased as deeper subshells were broached.

The forms of the charge state distributions indicate that the statistical weight from the number of pathways to each charge state appears to be a strongly defining factor. This suggests that combinatorial models based on simple physical reasoning could prove useful in predicting the general forms of the distributions.

By comparing the results from Xe with the study on Coulomb explosion of ICN in paper IV, we learned much about the relation between Auger cascades in atoms and related molecules. We saw that photoionization of the same subshells in Xe and I resulted in similar degree of ionization. This suggests that the inner-shell vacancies in ICN accrue and propagate upward in the energy level structure similarly to Xe when the ionizing orbitals are localized on iodine. This supports the model that deep molecular inner-shell vacancies, localized on heavy atoms, exhibit mostly atomic-like decays until the vacancies propagate to orbitals of predominantly molecular character.

Finally, in paper V, we explored the mechanisms involved in single-photon direct double ionization of He. We studied the sharing of kinetic energy between the two electrons as a function of the available excess energy, by systematically measuring the energy sharing distributions of the two electrons involved in the process. We developed a single-parameter empirical model to describe the behaviour of the energy sharing distributions. This model can be applied to other direct double ionization processes, and facilitates a method to compare other energy sharing distributions with the benchmarked case of He. We also demonstrated a method to separate and benchmark the partial KO and SO distributions from the measured total energy sharing distributions. The benchmarked KO and SO distributions allow comparison with related results of the two mechanisms in other atoms and molecules, and from other double ionization processes, such as direct double Auger decay.

Chapter 5

Outlook

A complex decay network, such as the Auger cascades of the heavy atoms studied in paper I and II, exemplifies some of the difficulties facing both modern experimental and computational methods. The two studies demonstrated the complexity involved when studying Auger cascades already by three-fold coincidences. Investigation of all steps involved in an Auger cascade that lead to higher than three-fold ionization would be more demanding from both an experimental and theoretical point of view. Experimental measurements of higher-dimensional coincidence data, demand a high level of understanding and control of how false coincidences may corrupt the data. Experiments would also have to run for significantly longer times to acquire sufficient statistics. This difficulty marks a vital point on the importance of instrumental development and improvement.

The key point where instrumental improvement would benefit research on Auger cascades would be the development of detectors with higher detection efficiency than the MCP plates used in this thesis. Recent detector developments have resulted in a new type of MCP plates with reported detection efficiencies up to 90% [65]. Upgrading the detector efficiency from about 50 to 90 % detection efficiency would significantly reduce the acquisition time required for multi-particle coincidence studies and would have a drastic, positive effect in reducing the influence of mixed coincidences. Furthermore, the studies on Cd and Hg relied on a resistively heated oven source to transform the sample from solid or liquid phase to gas phase. The current oven design can only operate at temperatures up to ∼500 °C before emission of thermal electrons from the oven causes problems. A continued study on Auger cascades in metal atoms hence necessitates development of ovens capable of operating at much higher temperatures than required for sublimating Cd and Hg.

Among the physical processes observed in this thesis, we studied the predicted rapid $4p^{-1}4d^{-1} \rightarrow 4d^{-3}$ decay in Cd. The process was observed for the decay chain $4s^{-1} \rightarrow 4p^{-1}4d^{-1} \rightarrow 4d^{-3}$, and the energy broadening was found to cover the entire span of energies between the binding energies of $4s^{-1}$ and $4d^{-3}$. Thus, we never observed the full broadening effect of the $4p^{-1}4d^{-1} \rightarrow 4d^{-3}$ decay. Suggestions have been put forward to instead study the $3d^{-1} \rightarrow 4p^{-1}4d^{-1} \rightarrow 4d^{-3}$ cascade to measure the full broadening effect [61]. The binding energy of the $3d^{-1}$ states is much higher compared to that of the $4s^{-1}$ hole, which would allow studying the decay of the $4p^{-1}4d^{-1}$ multiplet over a much larger energy interval. As both the $3d^{-1}$ and $4d^{-3}$ states are expected to be long-

lived, their relative influence on the total broadening of the $4p^{-1}4d^{-1} \rightarrow 4d^{-3}$ Auger line would be small. Studying this decay chain with a three-fold coincidence detection scheme would thus allow the estimation of the total lifetime of this very short-lived double hole state.

In general, studying Coster-Kronig transitions is an important part in the exploration of Auger cascades in atoms and molecules. Coster-Kronig transitions are mostly forbidden as the energy released when an inner-shell vacancy is filled by an electron from the same shell is generally not sufficient to release a secondary electron. However, when allowed, Coster-Kronig decays are expected to drastically influence the relaxation network of an inner-shell vacancy. Spectroscopic exploration and characterization of Coster-Kronig decays could therefore prove important for a complete understanding of Auger cascades and the endeavour of understanding Coulomb explosions and radiation damage.

In the year 2000, Neutze et. al. [66] predicted how radiation damage can dramatically affect structural studies of large biomolecules, probed by intense X-ray pulses. They proposed that the electrostatic energy caused by the number of produced charges expected from a high intensity X-ray FEL pulse, can lead to complete destruction of the molecule within the time-period of a 50 fs pulse. This exemplifies not only the time-scale and the effects of Auger cascades but also the importance of studying charge state distributions from inner-shell ionization. Benchmarked charge state productions from inner-shell vacancies could improve models on Coulomb explosions, as the number of positive charges drives the inter-nuclear dynamics responsible for radiation damage. It is therefore important to continue with multi-electron and multi-ion measurements, similar to the studies in papers I - IV, to deepen our understanding of the underlying mechanisms of Coulomb explosions.

The five studies presented in this thesis all have in common that they lack access to time-resolved information of the dynamics. The results are, instead, based primarily on the statistical outcome of the dynamical processes. With the advent of femto- and attosecond duration light sources, researchers now have the possibility to directly probe the dynamical aspects of processes such as molecular bond breaking and photoionization [67, 68]. Recent research performed by Månsson et. al. [68], at the Lund Laser Center, Sweden, also showed that attosecond XUV pulses could be used to directly study the time-dependent aspects of direct double photoionization of Xe, and separate the shake-off and knock-out mechanisms. Hopefully, in the not too distant future, one could use this fascinating technique to probe directly the time-dependent aspects of the energy sharing distributions in He, presented in paper V. In the near-future, the same methodology as we used in paper V could be applied to study the energy sharing distributions involved in direct double Auger decay and direct core-core, core-valence and

double-valence photoionization in other atoms and molecules. This could potentially shed new light on systematics and trends, which may be useful for our understanding of these less explored direct double ionization processes.

Bibliography

[1] D.J. Griffiths and D.F. Schroeter. *Introduction to quantum mechanics*. 3rd ed. Cambridge University Press, 2018.

[2] A. Kramida et al. *NIST Atomic Spectra Database.* (ver. 5.6.1), [Online] Available at: `https://physics.nist.gov/asd` [2019, April 17]. National Institute of Standards and Technology, Gaithersburg, MD. 2018.

[3] S. Johansson A. Thorne U. Litzen. *Spectrophysics: principles and applications*. Springer-Verlag Berlin Heidelberg, 1999.

[4] C. Froese Fischer, T. Brage, and P. Jönsson. *Computational atomic structure: an MCHF approach*. IOP Publishing Ltd. Bristol UK, 1997.

[5] B.H. Bransden and C.J. Joachain. *Physics of atoms and molecules*. 2nd ed. Pearson Education Limited, 2003.

[6] G. Wentzel. "Über strahlungslose Quantensprünge". In: *Z. Phys.* 43 (1927), p. 524.

[7] D. Chattarji. *The Theory of Auger Transitions*. Academic Press, New York, 1976.

[8] T.A. Carlson and M.O. Krause. "Experimental Evidence for Double Electron Emission in an Auger Process". In: *Phys. Rev. Lett.* 14 (1965), p. 390.

[9] E.J. McGuire. "Atomic L-Shell Coster-Kronig, Auger, and Radiative Rates and Flourescence Yields for Na-Th". In: *Phys. Rev. A* 3 (1971), p. 587.

[10] E.J. McGuire. "Atomic M-Shell Coster-Kronig, Auger, and Radiative Rates, and Fluorescence Yields for Ca-Th". In: *Phys. Rev. A* 5 (1972), p. 1043.

[11] E.J. McGuire. "Atomic N-shell Coster - Kronig, Auger, and radiative rates and fluorescence yields for $38 < Z < 103$". In: *Phys. Rev. A* 9 (1974), p. 1840.

[12] D. Coster and R. De L. Kronig. "New type of auger effect and its influence on the x-ray spectrum". In: *Physica* 2 (1935), p. 13.

[13] M. Ohno. "Strong Dynamical Effects in the X-Ray Photoemission Spectra and X-Ray Emission Spectra of the Elements Pd to Xe". In: *Physica Scripta* 21 (1980), p. 589.

[14] M. Ohno and G.A. van Riessen. "Hole-lifetime width: a comparison between theory and experiment". In: *Journal of Electron Spectroscopy and Related Phenomena* 128 (2003), p. 1.

[15] M.U. Kuchiev and S.A. Sheĭnerman. "Post-collision interaction in atomic processes". In: *Soviet Physics Uspekh* 32 (1989), p. 569.

[16] J.A.R. Samson et al. "Postcollision interactions in the Auger decay of the Ar L shell". In: *Phys. Rev. A* 54 (1996), p. 2099.

[17] J.A.R. Samson, Y. Lu, and W.C. Stolte. "Aspects of postcollision interactions near the Ar L shell". In: *Phys. Rev. A* 56 (1997), R2530.

[18] J.H.D. Eland. “Post-collision interaction and the Auger effect in double photoionisation of germanium compounds”. In: *Chemical Physics Letters* 409 (2005), p. 245.
[19] P. Lablanquie et al. “One photon double ionization of helium: threshold behaviour”. In: *Z. Phys. D* 16.77 (1990).
[20] R. Wehlitz et al. “Electron-energy and -angular distributions in the double photoionization of helium”. In: *Phys. Rev. Lett.* 67 (1991), p. 3764.
[21] J.M. Rost. “Quantum-classical hybrid approach to helium double photoionization”. In: *Phys. Rev. A* 53 (1996), R640.
[22] R. Dörner et al. “Fully Differential Cross Sections for Double Photoionization of He Measured by Recoil Ion Momentum Spectroscopy”. In: *Phys. Rev. Lett.* 77 (1996), p. 1024.
[23] A. Knapp et al. “Mechanisms of Photo Double Ionization of Helium by 530 eV Photons”. In: *Phys. Rev. Lett.* 89 (2002), p. 033004.
[24] T. Schneider, P.L. Chocian, and J.M. Rost. “Separation and Identification of Dominant Mechanisms in Double Photoionization”. In: *Phys. Rev. Lett.* 89 (2002), p. 073002.
[25] T. Schneider and J.M. Rost. “Double photoionization of two-electron atoms based on the explicit separation of dominant ionization mechanisms”. In: *Phys. Rev. A* 67 (2003), p. 062704.
[26] T. Pattard, T. Schneider, and J.M. Rost. “On the role of shake-off in single-photon double ionization”. In: *Journal of Physics B: Atomic, Molecular and Optical Physics* 36 (2003), p. L189.
[27] T. Pattard and J. Burgdörfer. “Half-collision model for multiple ionization by photon impact”. In: *Phys. Rev. A* 64 (2001), p. 042720.
[28] J.M. Rost. “Two-electron escape near threshold: a classical problem?” In: *Phys. Rev. Lett.* 72 (1994), p. 1998.
[29] M. Ya. Amusia et al. “Two-electron photoionization of helium”. In: *Journal of Physics B: Atomic and Molecular Physics* 8 (1975), p. 1248.
[30] M.S. Schöffler et al. “Ejection of Quasi-Free-Electron Pairs from the Helium-Atom Ground State by Single-Photon Absorption”. In: *Phys. Rev. Lett.* 111 (2013), p. 013003.
[31] A. Einstein. “On a heuristic point of view concerning the production and transformation of light”. In: *Ann. d. Phys., 17* (1905), p. 132.
[32] *Beam line UE52-SGM*. [Online] Available at: `https://www.helmholtz-berlin.de/pubbin/igama_output?modus=einzel&sprache=en&gid=1639&typoid=35512` [2019, April 18].
[33] P. Miedema et al. “The variable polarization undulator beamline UE52 SGM at BESSY II”. In: *Journal of large-scale research facilities* 2 (2016), A70.
[34] *Beam line U49-2*. [Online] Available at: `https://www.helmholtz-berlin.de/pubbin/igama_output?modus=einzel&sprache=en&gid=1655&typoid=35512` [2019, April 18].

[35] J.A. Bearden and A.F. Burr. "Reevaluation of X-Ray Atomic Energy Levels". In: *Rev. Mod. Phys.* 39 (1967), p. 125.
[36] *Photoemission in Solids I: General Principles*. Springer-Verlag, Berlin, 1978.
[37] J.C. Fuggle and N. Mårtensson. "Core-level binding energies in metals". In: *Journal of Electron Spectroscopy and Related Phenomena* 21 (1980), p. 275.
[38] David Attwood. *Soft X-rays and Extreme Ultraviolet Radiation, principles and applications*. Cambridge University Press, 1999.
[39] J.H.D. Eland et al. "Complete two-electron spectra in double photoionization: The rare gases Ar, Kr, and Xe". In: *Physical Review Letters* 90 (2003), p. 053003.
[40] S. Plogmaker et al. "Versatile high-repetition-rate phase-locked chopper system for fast timing experiments in the vacuum ultraviolet and x-ray spectral region". In: *Review of Scientific Instruments* 83 (2012), p. 013115.
[41] W.C. Wiley and I.H. McLaren. In: *Review of Scientific Instruments* 26 (1955), p. 1150.
[42] A.T.J.B. Eppink and D.H. Parker. "Velocity map imaging of ions and electrons using electrostatic lenses: Application in photoelectron and photofragment ion imaging of molecular oxygen". In: *Review of Scientific Instruments* 68 (1997), p. 3477.
[43] J.H.D Eland. et al. "Dissociation of multiply charged ICN by Coulomb explosion". In: *The Journal of Chemical Physics* 145 (2016), p. 074303.
[44] V. Zhaunerchyk et al. "Theory and simulations of covariance mapping in multiple dimensions for data analysis in high-event-rate experiments". In: *Phys. Rev. A* 89 (2014), p. 053418.
[45] L. J. Frasinski, K. Codling, and P. A. Hatherly. "Covariance Mapping: A Correlation Method Applied to Multiphoton Multiple Ionization". In: *Science* 246 (1989), p. 1029.
[46] L.J. Frasinski et al. "Dynamics of Hollow Atom Formation in Intense X-Ray Pulses Probed by Partial Covariance Mapping". In: *Phys. Rev. Lett.* 111 (2013), p. 073002.
[47] E. Andersson et al. "Formation of Kr^{3+} via core-valence doubly ionized intermediate states". In: *Physical Review A* 85 (2012), p. 032502.
[48] Y. Hikosaka et al. "Single, double, and triple Auger decay of the Xe 4p core-hole states". In: *Physical Review A* 76 (2007), p. 032708.
[49] P. Linusson et al. "Single-photon multiple ionization forming double vacancies in the 2p subshell of argon". In: *Physical Review A* 87 (2013), p. 043409.
[50] P. Linusson et al. "Complete double valence photoionization study of the electron spectra of krypton". In: *Physical Review A* 88 (2013), p. 022510.
[51] J. Palaudoux et al. "Multielectron spectroscopy: Auger decays of the krypton 3d hole". In: *Physical Review A* 82 (2010), p. 043419.
[52] M. Huttula et al. "Spectroscopy of triply and quadruply ionized states of mercury". In: *Physical Review A* 83 (2011), p. 032510.
[53] P. Linusson et al. "Double ionization of atomic cadmium". In: *Physical Review A* 83 (2011), p. 023424.

[54] M. Huttula et al. “Core-valence double photoionization of atomic mercury”. In: *Phys. Rev. A* 89 (2014), p. 013411.

[55] J. Palaudoux et al. “Auger decay paths of mercury $5p$ and $4f$ vacancies revealed by multielectron spectroscopy”. In: *Phys. Rev. A* 91 (2015), p. 012513.

[56] S. Svensson et al. “Lifetime broadening and CI-resonances observed in ESCA”. In: *Phys. Scr.* 14 (1976), p. 141.

[57] M. Ohno. “Strong dynamical effects in unusually broad $L_{\gamma 2,3}$ emission spectra of $_{46}$Pd to $_{54}$Xe”. In: *Journal of Physics C: Solid State Physics* 13 (1980), p. 447.

[58] M. Ohno and J-M. Mariot. “Many-electron interactions in the M_{45}-NN Auger spectrum of metallic cadmium”. In: *Journal of Physics C* 14 (1981), p. L1133.

[59] F.A. Parpia, C. Froese Fischer, and I.P. Grant. “GRASP92: A package for large-scale relativistic atomic structure calculations”. In: *Computer Physics Communications* 94 (1996), p. 249.

[60] S. Fritzsche. “The Ratip program for relativistic calculations of atomic transition, ionization and recombination properties”. In: *Computer Physics Communications* 183 (2012), p. 1525.

[61] M. Ohno. “Many-body effect in the M_{45}–$N_{23}N_{45}$–$N_{45}N_{45}N_{45}$ coincidence spectroscopy spectra of metallic elements around Cd”. In: *Journal of Electron Spectroscopy and Related Phenomena* 160 (2007), p. 15.

[62] H. Aksela and S. Aksela. “$N_{4,5}$ $N_{6,7}$ X Coster-Kronig spectra of free Hg atoms”. In: *Journal of Physics B: Atomic and Molecular Physics* 16 (1983), p. 1531.

[63] J.A.D. Matthew, F.P. Netzer, and E. Bertel. “The $N_{4,5}$ $N_{6,7}$ $N_{6,7}$ and $N_{4,5}N_{6,7}O_{4,5}$ Auger spectra of Au, Pt and Ir”. In: *Journal of Electron Spectroscopy and Related Phenomena* 20 (1980), p. 1.

[64] T.A. Carlson and R.M. White. “Measurement of the Relative Abundances and Recoil-Energy Spectra of Fragment Ions Produced as the Initial Consequences of X-Ray Interaction with CH_3I, HI, and DI”. In: *The Journal of Chemical Physics* 44 (1966), p. 4510.

[65] K. Fehre et al. “Absolute ion detection efficiencies of microchannel plates and funnel microchannel plates for multi-coincidence detection”. In: *Review of Scientific Instruments* 89 (2018), p. 045112.

[66] R. Neutze et al. “Potential for biomolecular imaging with femtosecond X-ray pulses”. In: *Nature* 406 (2000), p. 752.

[67] R.J. Squibb et al. “Acetylacetone photodynamics at a seeded free-electron laser”. In: *Nature Communications* 9 (2018), p. 63.

[68] E.P. Månsson et al. “Double ionization probed on the attosecond timescale”. In: *Nature Physics* 10 (2014), p. 207.

Acknowledgements

My years as a doctoral student have been filled with great experiences. I have met and worked with fantastic people from all around the globe, and I have learnt so much from everyone who's crossed paths with me during these years. It has been a truly inspiring time, and I will always be grateful for these years.

Most of my time working on this thesis has been spent in Sweden, at my office in Gothenburg. I have been fortunate to work in a great environment, with amazing people at the Department of Physics at Gothenburg University. I have many people to thank for my time as a doctoral student. I would first of all like to express my appreciation to everyone on level 8 in Forskarhuset, whom I have met in the corridors on a daily basis. Many people have come and gone during the years, and it has been a pleasure to get to know so many of you.

I would also like to give a special thanks to my co-supervisor Dag Hanstorp for introducing me to the weekly Thursday-innebandy sessions, and to Jonathan Weidow for firing up the enthusiasm for it every week. You showed me that I am not the only physicist who's as passionate about silly sports, as about spherical particles in vacuum. I would also like to express my deep gratitude to the administrative staff, especially to Bea Tensfeldt, Maria Siirak, Clara Wilow Sundh and Pernilla Larsson for your help, regardless of the type of doctoral student-related mess there was. You deserve a big thank you!

The work in this thesis is a result of hard work of many talented people. During the years, we as a research group have performed experiments at large scale experimental facilities in Germany, France and Italy. These experiments would never have been possible without the help from collaborators from other experimental research groups and from local staff and beam-line scientists at BESSY II in Berlin, SOLEIL in Paris, and FERMI in Trieste. I would also like to mention and thank Jan-Åke Wiman for all his technical support over the years.

The results in this thesis would also never have been possible without collaboration with theoretical researchers. I would therefore like to thank Randolf Beerwerth and professor Stefan Fritzsche for a long lasting and successful collaboration. I would also like to thank professor Jan-Michael Rost for sharing his expertise and for inviting me to work in Dresden. I want to mention my other co-supervisor Vitali Zhaunerchyk, for sharing his knowledge in physics and data analysis. I have learnt a lot from you, and I have really appreciated our discussions over the years.

Of course, I want to thank my fantastic team members for all these years. We have experienced so much together, and it has been wonderful to work with all of you. We have worked together, travelled together and spent numerous day and night shifts together acquiring data in our home lab and during all beam times in Berlin, Paris and Trieste. You have given me five fantastic years of my life, and filled them with great memories every day. A *huge* thank you to Richard, Andreas, Dimitris, Raj, Sergey, Craig, Omid, Måns and all bachelor and master students who has been in our group during these years. And Richard, it is hard to describe how much we all appreciate your enormous knowledge, kindness and desire to help everyone. Thank you for everything! Also, Vasyl and Ray, thank you for bringing so much fun everyday, especially during all our great lunch conversations, filled with both interesting and entertaining discussions.

After all, I would never have had the chance to meet all these fantastic people if it wasn't for my main supervisor Raimund Feifel. Raimund, you have been a fantastic supervisor and I have learnt so much from you. I will never forget the day of my interview and how happy I was when you called me on the phone to offer the position. It is hard to grasp that five years have passed since then. These years have been an important part of my life, and I have you to thank for it. I also want to thank you for introducing me to the expert, John Eland. John, I have admired your knowledge and your never ending curiosity since I first met you. It has been truly inspiring to work so closely with you, and I want to thank you for everything you have taught me.

Ten years has passed since I started studying physics. It has been a long journey which would have never been possible without all of my friends and the love and support I have from my family. Tack för att ni finns!

Last but not least, words cannot express my gratefulness to you, Angelika. Everyday, you fill my life with so much love and joy. Nothing compares walking through life with you. You are my greatest source of inspiration, my best friend and my love. None of this would have been possible without you.

Jonas Andersson, May 2019